1 **FRONT MATTER**

2 **Title**

3 Mid-Holocene Antarctic sea-ice increase driven by marine ice sheet retreat

4 **Authors**

5 Kate E. Ashley[1], Robert McKay[2], Johan Etourneau[3], Francisco J. Jimenez-Espejo[3,4], Alan Condron[5],

6 Anna Albot[2], Xavier Crosta[6], Christina Riesselman[7,8], Osamu Seki[9], Guillaume Massé[10], Nicholas R.

7 Golledge[2,11], Edward Gasson[12], Daniel P. Lowry[2,11], Nicholas E. Barrand[1], Katelyn Johnson[2], Nancy

8 Bertler[2,11], Carlota Escutia[3], Robert Dunbar[13] and James A. Bendle[1*].

9 **Affiliations**

10 [1]School of Geography, Earth and Environmental Sciences, University of Birmingham, Edgbaston,

11 Birmingham, B15 2TT, UK

12 [2]Antarctic Research Centre, Victoria University of Wellington, Wellington 6140, New Zealand

13 [3]Instituto Andaluz de Ciencias de la Tierra (CSIC), Avenida de las Palmeras 4, 18100 Armilla, Granada,

14 Spain

15 [4]Department of Biogeochemistry, Japan Agency for Marine-Earth Science and Technology

16 (JAMSTEC), Yokosuka 237-0061, Japan

17 [5]Department of Geology and Geophysics, Woods Hole Oceanographic Institution, Woods Hole, MA

18 02543, USA

19 [6]UMR-CNRS 5805 EPOC, Université de Bordeaux, 33615 Pessac, France

20 [7]Department of Geology, University of Otago, Dunedin 9016, New Zealand

21 [8]Department of Marine Science, University of Otago, Dunedin 9016, New Zealand

22 [9]Institite of Low Temperature Science, Hokkaido University, Sapporo, Hokkaido, Japan

23 [10]TAKUVIK, UMI 3376 UL/CNRS, Université Laval, 1045 avenue de la Médecine, Quebec City,

24 Quebec, Canada G1V 0A6

25 [11]GNS Science, Avalon, Lower Hutt 5011, New Zealand

26 [12]Department of Geography, University of Sheffield, Winter Street, Sheffield, S10 2TN, UK

27 [13]Department of Environmental Earth Systems Science, Stanford University, Stanford, A 94305-2115

29 [*]**Corresponding Author:** email: j.bendle@bham.ac.uk

1. ABSTRACT

Over recent decades Antarctic sea-ice extent has increased, alongside widespread ice shelf thinning and freshening of waters along the Antarctic margin. In contrast, Earth system models generally simulate a decrease in sea ice. Circulation of water masses beneath large cavity ice shelves is not included in current Earth System models and may be a driver of this phenomena. We examine a Holocene sediment core off East Antarctica that records the Neoglacial transition, the last major baseline shift of Antarctic sea-ice, and part of a late-Holocene global cooling trend. We provide a multi-proxy record of Holocene glacial meltwater input, sediment transport and sea-ice variability. Our record, supported by high-resolution ocean modelling, shows that a rapid Antarctic sea-ice increase during the mid Holocene (~4.5 ka) occurred against a backdrop of increasing glacial meltwater input and gradual climate warming. We suggest that mid-Holocene ice shelf cavity expansion led to cooling of surface waters and sea-ice growth which slowed basal ice shelf melting. Incorporating this feedback mechanism into global climate models will be important for future projections of Antarctic changes.

44

2. INTRODUCTION

Ice shelves and sea ice are intrinsically linked and represent fundamental components of the global climate system, impacting ice-sheet dynamics, large-scale ocean circulation, and the Southern Ocean biosphere. Antarctic ice-shelves with large sub-shelf cavities (e.g. Ross, Filchner-Ronne) play a key role in regional sea-ice variations, by cooling and freshening surface ocean waters for hundreds of kilometres beyond the ice shelf edge (Hellmer, 2004; Hughes *et al.*, 2014). Antarctic sea ice has expanded over the past few decades, particularly in the western Ross Sea region (Turner *et al.*, 2016), alongside widespread thinning of ice shelves (Paolo *et al.*, 2015) and freshening along the Antarctic margin (Jacobs *et al.*, 2002; Aoki *et al.*, 2013). The drivers and feedbacks involved in these decadal trends are still poorly understood, hampered by the sparse and short-term nature of meteorological, oceanographic and glaciological observations (Jones *et al.*, 2016), and thus establishing the long-term trajectory for East Antarctic sea ice on the background of accelerated ice sheet loss remains a challenge. Marine sediment cores provide a longer-term perspective and highlight a major baseline shift in coastal sea ice ~4.5 ka ago (Steig *et al.*, 1998; Crosta *et al.*, 2008; Denis *et al.*, 2010) which characterizes the mid-Holocene 'Neoglacial' transition in the Antarctic. A mechanistic driver for this climate shift currently remains

60   unresolved, but we propose that two interrelated aspects of the last deglaciation are significantly

61   underrepresented in current models of this transition: (i) the retreat of grounded ice sheets from the

62   continental shelves of Antarctica, and (ii) the subsequent development of large ice shelf cavities during

63   the Holocene. Both factors would significantly alter water mass formation on Antarctica's continental

64   shelves, which today are major source regions of Antarctic Bottom Water (AABW) and Antarctic

65   Surface Water (AASW). These interrelated processes are underrepresented in coupled ocean-atmosphere

66   models which currently do not simulate the timing, magnitude and rapid onset of the Neoglacial

67   (Supplementary Materials).

68

69   Integrated Ocean Drilling Program (IODP) Expedition 318 cored a 171 m thick deposit of laminated

70   diatomaceous ooze at Site U1357 offshore Adélie Land (Fig. 1), deposited over the past 11,400 years.

71   Here, we present a new Holocene record of glacial meltwater, sedimentary input and local sea ice

72   concentrations from Site U1357 using compound-specific hydrogen isotopes of fatty acid biomarkers

73   (δ^2H_{FA}), terrigenous grain size (mud percent, sorting), natural gamma radiation, biogenic silica

74   accumulation, highly-branched isoprenoid alkenes (HBIs) and Ba/Ti ratios (Fig. 4 and 5).

75

76   We interpret δ^2H_{FA} (Fig. 4a) fluctuations in Adélie Drift sediments as a record of meltwater input from

77   isotopically-depleted glacial ice. Antarctic glacial ice is highly depleted in ^2H compared to ocean water,

78   thus creating highly contrasting end-member values for the two major H source pools. Grain size,

79   natural gamma radiation (NGR) and terrigenous and biosiliceous mass accumulation rates (MARs)

80   reflect changing sediment delivery either driven via local glacial meltwater discharge or advection of

81   suspended sediment by oceanic currents. The diene/triene HBI ratio is used as a proxy for coastal sea ice

82   presence (Massé *et al.*, 2011). Ba/Ti enrichment is considered to reflect enhanced primary productivity.

83   These records allow a unique opportunity to reconstruct the magnitude of the coupled response of the

84   ocean and ice sheet during the Neoglacial transition. Details on all proxies and associated uncertainties

85   can be found in Section S2 of the Supplementary Information.

86

87

88   **3. MATERIALS AND METHODS**

89

90   **3.1 Organic geochemical analyses**

3.1.1 Fatty acid extraction

Lipid extraction of sediment samples was performed at the Royal Netherlands Institute for Sea Research (NIOZ). Freeze-dried and homogenized samples were extracted by Dionex™ accelerated solvent extraction (DIONEX ASE 200) using a mixture of dichloromethane (DCM)/methanol (MeOH) (9:1, v/v) at a temperature of 100°C and a pressure of 7.6×10^6 Pa (Kim *et al.*, 2010).

Compound separation was undertaken at University of Glasgow, UK. The total lipid extract was separated over an aminopropyl silica gel column and the total acid fraction was eluted into an 8ml vial with 4% acetic acid in ethyl-ether solution (Huang *et al.*, 1999). Derivatisation to Fatty Acid Methyl Esters was achieved by adding 200 μl of MeOH containing 14% v/v Boron triflouride to the 8ml vial containing the TAF. FAMES were recovered and cleaned up by eluting through a pre-cleaned 3cm silica gel column (60 A; 35-70) with 4ml of hexane and 4ml of DCM (containing the FAMES). δ^2H values indicate depletion against the international standards: Vienna Pee Dee Belemnite (V-PDB) is the standard for δ13C and Vienna Standard Mean Ocean Water (V-SMOW) for δ^2H.

3.1.2 Fatty acid hydrogen isotope analysisCompound specific hydrogen isotope analyses of FAMES was performed at the Institute of Low Temperature Science, Hokkaido University. δ^2H values were obtained using a CS-IRMS system with a HP 6890 gas chromatograph and a ThermoQuest Finnigan MAT Delta Plus XL mass spectrometer. Separation of the FAMES was achieved with a HP-5 MS fused silica capillary column (30 m x 0.32 mm i.d., film thickness of 0.25 μm) with a cooled on-column injector. An *n*-alkane and a reference gas whose isotopic values were known was co-injected with the samples as an internal isotopic standard for δ^2H. A laboratory standard (Mix F8 of FAMES from Indiana University) containing C_{10}–C_{30} FAMES was analyzed daily to check the accuracy and the drift of the instrument and to normalize the data to the SMOW/SLAP isotopic scale. The H^{3+} factor was measured every three days.

3.1.3 HBIs

Highly branched isoprenoids (HBI) alkenes were extracted at Laboratoire d'Océanographie et du Climat: Experimentations et Approches Numériques (LOCEAN), separately from the fatty acids, using a mixture of 9mL CH_2Cl_2/MeOH (2:1, v:v) to which 7 hexyl nonadecane (m/z 266) was added as an internal standard, following the Belt et al (2007) and Massé et al. (2011) protocols. Several sonication and centrifugation steps were applied in order to properly extract the selected compounds (Etourneau *et*

122 *al.*, 2013). After drying with N_2 at 35°C, the total lipid extract was fractionated over a silica column into

123 an apolar and a polar fraction using 3 mL hexane and 6 mL CH_2Cl_2/MeOH (1:1, v:v), respectively. HBIs

124 were obtained from the apolar fraction by the fractionation over a silica column using hexane as eluent

125 following the procedures reported by Belt *et al.* (2007; Massé *et al.*, 2011). After removing the solvent

126 with N_2 at 35°C, elemental sulfur was removed using the TBA (Tetrabutylammonium) sulfite method

127 (Jensen *et al.*, 1977; Riis and Babel, 1999). The obtained hydrocarbon fraction was analyzed within an

128 Agilent 7890A gas chomatograph (GC) fitted with 30 m fused silica Agilent J&C GC column (0.25 mm

129 i.d., 0.25 µm film thickness), coupled to an Agilent 5975C Series mass selective detector (MSD).

130 Spectra were collected using the Agilent MS-Chemstation software. Individual HBIs were identified on

131 the basis of comparison between their GC retention times and mass spectra with those of previously

132 authenticated HBIs (Johns *et al.*, 1999) using the Mass Hunter software. Values are expressed as

133 concentration relative to the internal standard.

134

135 **3.2 Inorganic geochemical analysis and electronic microscopy**

136 Major element concentrations were obtained using X-Ray Fluorescence Scanner on 412 analyses

137 measured directly over undisturbed sediment sections. The bulk major element composition included in

138 this study was measured between sections U1357B-1H-2 to U1357-19H-5 continuously each 50 cm. We

139 used an Avaatech X-ray fluorescence (XRF-Scanner) core scanner at the IODP-Core Repository/Texas

140 A&M University laboratories (USA) during December 2010. Non-destructive XRF core-scanning

141 measurements were performed over 1 cm^2 area with slit size of 10 mm, a current of 0.8 mA and

142 sampling time of 45 seconds at 10 kV in order to measure the relative content of titanium (Ti) and

143 barium (Ba).

144

145 Field emission scanning electron microscopy (FESEM) images and corresponding spectrum were

146 obtained with an AURIGA FIB-FESEM Carl Zeiss SMT at Centro de Instrumentación Científica,

147 Granada University, Spain

148

149 **3.3 Grain size analyses**

150 A total of 341 samples were prepared for grain size analysis. Samples were treated for removal of

151 biogenic opal with a 1M sodium hydroxide NaOH solution and incubated in a water bath at 80°C for 24

152 hours. This procedure was repeated twice due to an incomplete dissolution of diatoms observed in smear

153   slides. The samples were then treated with H_2O_2 to remove organic material at 80°C for 24 hours.

154   Samples were measured using a Beckman Coulter LS 13 320 Laser Diffraction Particle Size Analyser

155   (LPSA). Prior to grain size analysis, ~30 mL of 0.5 g/L Calgon (sodium hexametaphosphate) was added

156   to the samples, and sonicated and stirred in order to disperse the grains and prevent clumping.

157

3.4 Biogenic silica

159   Biogenic silica concentrations (wt% BSi) were measured on 349 discrete samples using a molybdate

160   blue spectrophotometric method modified from (Strickland and Parsons, 1970; DeMaster, 1981).

161   Analytical runs included replicates from the previous sample group and from within the run, and each

162   run was controlled by 10 standards and a blank with dissolved silica concentrations ranging from 0 µM

163   to 1200 µM. For each analysis, ~7 mg of dry, homogenized sediment was leached in 0.1M NaOH at

164   85°C, and sequential aliquots were collected after 2, 3, and 4 hours. Following addition of reagents,

165   absorbance of the 812 nm wavelength was measured using a Shimadzu UV-1800 spectrophotometer.

166   Dissolved silica concentration of each unknown was calculated using the standard curve, and data from

167   the three sampling hours were regressed following the method of DeMaster (1981) to calculate wt%

168   BSi. In our U1357B samples, wt% BSi ranges from maximum of ~60% in early and mid-Holocene light

169   laminae to a minimum of 31% in late Holocene dark laminae. The average standard deviation of

170   replicate measurements is 0.5%.

171

3.5 Model simulations

173   All numerical calculations were performed using the Massachusetts Institute of Technology general

174   circulation model (MITgcm) (Marshall *et al.*, 1997); a three-dimensional, ocean sea-ice, hydrostatic,

175   primitive equation model. The experiments presented here were integrated on a global domain projected

176   onto a cube-sphere grid to permit a relatively even grid spacing and to avoid polar singularities (Adcroft

177   *et al.*, 2004; Condron and Winsor, 2012). The ocean grid has a mean, eddy-permitting, horizontal grid

178   spacing of 1/6° (18-km) with 50 vertical levels ranging in thickness from 10m near the surface to

179   approximately 450m at the maximum model depth. The ocean model is coupled to a sea-ice model in

180   which ice motion is driven by forces generated by the wind, ocean, Coriolis force, and surface elevation

181   of the ocean, while internal ice stresses are calculated using a viscous-plastic (VP) rheology, as

182   described in Zhang and Hibler (1997). In all experiments, the numerical model is configured to simulate

183   present-day (modern) conditions: Atmospheric forcings (wind, radiation, rain, humidity etc.) are

prescribed using 6-hourly climatological (1979-2000) data from the ERA-40 reanalysis product produced by the European Centre for Medium-range Weather Forecasts and background rates of runoff from the ice sheet to the ocean are based on the numerical ice sheet model of Pollard and Deconto (2016) integrated over the same period (1979-2000). To study the pathway of meltwater in the ocean, additional fresh (i.e. 0 psu) water was released into the surface layer of the ocean model at the grid points closest to the front of the Ross Ice Shelf. Five different discharge experiments were performed by releasing meltwater into this region at rates of 0.01 Sv (Sv = 10^6 m3/s), 0.05 Sv, 0.1 Sv, 0.5 Sv, and 1 Sv for the entire duration of each experiment (~3.5 years).

4. ENVIRONMENTAL SETTING AND INTERPRETATION OF PROXY DATA

We utilize a 180 m thick sediment core that was recovered from the Wilkes Land Margin continental shelf in the Adélie Basin (IODP Site U1357). This core targeted an expanded sediment drift (Adélie Drift) and provides a high-resolution Holocene record of climate variability. Below we provide pertinent details on this unique site and on our application of compound specific δ^2H measurements on algal biomarkers as a novel meltwater proxy. Further details on proxy interpretation (Ba/Ti, grain size, HBIs) are given in the Supplementary Materials.

4.1 The Adélie Drift

Site U1357 is located in the Dumont d'Urville Trough of the Adélie Basin, ca. 35 km offshore from Adélie Land (66°24.7990'S, 140°25.5705'E; Fig 1). This is a >1000 m deep, glacially scoured depression on the East Antarctic continental shelf, bounded to the east by the Adélie Bank. Further east lays the Adélie Depression and the Mertz Bank, the latter located north of the Mertz Glacier floating ice tongue. The Adélie Land region is dissected by several glaciers which could potentially contribute terrigenous sediment into the coastal zone with the core site located 40 km to the north of the Astrolabe Glacier, and ca. 75 and 300 km northwest of the Zélée and Mertz glaciers, respectively.

The site itself is located within the Dumont d'Urville polynya (DDUP), which has a summer (winter) extent of 13,020 km^2 (920 km^2), but is also directly downwind and downcurrent of the much larger and highly productive Mertz Glacier polynya (MGP) to the east, with a summer (winter) extent of 26,600 km^2 (591 km^2) (Arrigo and van Dijken, 2003). The MGP forms as a result of reduced sea-ice westward advection due to the presence of the Mertz Glacier Tongue (Massom *et al.*, 2001) and strong katabatic

215   winds which blow off the Antarctic ice sheet with temperatures below -30°C (Bindoff *et al.*, 2000).

216   Katabatic winds freeze the surface waters and blow newly formed ice away from the coast, making the

217   polynya an efficient sea-ice 'factory', with higher rates of sea-ice formation in comparison to non-

218   polynya ocean areas which undergo seasonal sea ice formation (Kusahara *et al.*, 2010). The MGP

219   produces 1.3% of the total Southern Ocean sea ice volume despite occupying less than 0.1% of total

220   Antarctic sea ice extent (Marsland *et al.*, 2004).

221

222   As a result of the upwelling polynya environments, the area along the Adélie Coast is characterized by

223   extremely high primary productivity, with the water column known to host significant amounts of

224   phytoplankton, dominated by diatoms (Beans *et al.*, 2008). The Mertz Glacier zone is generally

225   characterized by stratified waters in the summer, due to seasonal ice melt, with these conditions

226   corresponding to the highest phytoplankton biomass. The lack of ice cover means polynyas are the first

227   polar marine systems exposed to spring solar radiation, making them regions of enhanced biological

228   productivity compared to adjacent waters. A considerable amount of resultant sedimentation is focused

229   via the westward flowing currents from both of these polynyas within the deep, protected Adélie Basin,

230   resulting in a remarkably high sedimentation rate of ca. 1.5-2 cm year^{-1} at Site U1357 (Escutia *et al.*,

231   2011).

232

233   Although biogenic and terrigenous sediment is interpreted to be sourced locally in the Adélie Land

234   region, the mass accumulation rate of these sediments in this drift is associated with the intensity of

235   westward flowing currents (S2.2). Critically, these westward currents also act to transport water masses

236   from further afield, and Site U1357 is directly oceanographically downstream of the Ross Sea, meaning

237   the continental shelf in this region receives significant Antarctic Surface Water (ASSW) transported by

238   the Antarctic Slope Current (ASC) and Antarctic Coastal Current from the Ross Sea embayment . Thus,

239   changes in the surface waters of the Ross Sea influence Site U1357. Whitworth et al. (1998) confirm the

240   continuity of the westward flowing ASC between the Ross Sea and the Wilkes Land margin. This flow

241   is largely associated with the Antarctic Slope Front, which reflects the strong density contrast between

242   AASW and Circumpolar Deep Water (CDW). McCartney and Donohue (2007) estimate that the

243   transport in the westward ASC, which links the Ross Sea to the Wilkes Land margin, reaches 76 Sv (Sv

244    $= 10^6$ m^3 s^{-1}). However, Peña-Molino et al. (2016) measured a highly variable ASC flow at 113°E

245   ranging from 0 to 100 Sv with a mean of 21.2 Sv. This contributes to a cyclonic gyre, which together

246   with the ASC dominate the circulation at Site U1357. The gyre transport is around 35 Sv, and comes

247   mainly from the Ross Sea region, with a lesser contribution from a westward flow associated with the

248   Antarctic Circumpolar Current (McCartney and Donohue, 2007).

249

250   **4.2 Site specific interpretation of $\delta^2 H_{FA}$ as a glacial meltwater proxy**

251

252   **4.2.1. Source of fatty acids**

253   To best interpret the hydrogen isotope signal recorded by the C_{18} FA, it is important to determine the

254   most likely source these compounds are derived from, and thus the habitat in which they are produced.

255   The C_{18} FA, however, is known to be produced by a wide range of organisms and so we cannot preclude

256   the possibility of multiple sources, especially in a highly diverse and productive region such as the

257   surface waters of offshore Adélie Land. However, we can attempt to determine the most dominant

258   producer(s), which will help us understand the main signal being recorded by the isotopes.

259

260   An analysis of the FAs within eight classes of microalgae by Dalsgaard *et al.* (2003) (compiling results

261   from multiple studies) showed *Cryptophyceae, Chlorophyceae, Prasinophyceae* and *Prymnesiophyceae*

262   to be the most dominant producers of total C_{18} FAs. The *Bacillariophyceae* class, on the other hand,

263   which includes the diatoms, were found to produce only minor amounts of C_{18} FA, instead synthesizing

264   abundant $C_{16:1}$ FAs. Thus, despite the water column offshore Adélie Land being dominated by diatoms,

265   these are unlikely to be a major source of the C_{18} FA within U1357B (Beans *et al.*, 2008; Riaux-Gobin

266   *et al.*, 2011).

267

268   Of the four microalgae classes dominating C_{18} production (Dalsgaard *et al.*, 2003), species from the

269   Chlorophyceae and Prymnesiophyceae classes have been observed within surface waters offshore

270   Adélie Land after spring sea-ice break-up (Riaux-Gobin *et al.*, 2011). Here, *Phaeocystis antarctica* of

271   the Prymnesiophytes was found to dominate the surface water phytoplankton community (representing

272   16% of the phytoplankton assemblage), whereas Cryptophyceae spp. were found in only minor

273   abundances (Riaux-Gobin *et al.*, 2011). In the Antarctic, *Phaeocystis* is thought to be the most dominant

274   producer of C_{18} FAs (Dalsgaard *et al.*, 2003), and thus is likely to be a key producer of the C_{18} FA in

275   U1357B samples.

276

277 To investigate this further, we measured compound-specific carbon isotopes of the C_{18} FAs in U1357B

278 samples, which gives an average $\delta^{13}C$ value of -29.8 ± 1.0 ‰ (n=85). Budge *et al.* (2008) measured a

279 similar $\delta^{13}C$ value of -30.7 ± 0.8‰ from C_{16} FAs derived from Arctic pelagic phytoplankton, while sea

280 ice algae and higher trophic level organisms all had much higher $\delta^{13}C$ values (sea ice algae having

281 values of -24.0 ± 2.4‰). Assuming similar values apply for the C_{18} FA and for organisms within the

282 water column at our site, this suggests that our C_{18} FA is predominantly derived from pelagic

283 phytoplankton.

284

285 Furthermore, $\delta^{13}C$ measurements of suspended particulate organic matter (SPOM) near Prydz Bay, East

286 Antarctica by Kopczynska *et al.* (1995) showed that sites with high $\delta^{13}C$ SPOM values (-20.1 to -

287 22.4‰) were characterized by diatoms and large heterotrophic dinoflagellates, whereas the lowest $\delta^{13}C$

288 SPOM values (-29.7 to -31.85‰) were associated with *Phaeocystis*, naked flagellates and autotrophic

289 dinoflagellates. Wong and Sackett (1978) measured the carbon isotope fractionation of seventeen

290 species of marine phytoplankton and showed that Haptophyceae (of which *Phaeocystis* belongs) had the

291 largest fractionation of -35.5‰.

292

293 Therefore, based on the known producers of C_{18} FAs, observed phytoplankton assemblages within

294 modern surface waters offshore Adélie Land, and the $\delta^{13}C$ value of C_{18} FAs in U1357B samples, as

295 discussed above, we argue that the C_{18} FA here is predominantly produced by *Phaeocystis* (most likely

296 *P. antarctica*), but with potential minor inputs from other algal species such as Cryptophytes or diatoms.

297

298 *Phaeocystis antarctica* is a major phytoplankton species within the Antarctic, dominating spring

299 phytoplankton blooms, particularly in the Ross Sea (DiTullio *et al.*, 2000; Schoemann *et al.*, 2005). It is

300 known to exist both within sea ice and in open water (Riaux-Gobin et al., 2013) and has been observed

301 in surface waters in great abundance following spring sea-ice break-up, at both coastal and offshore sites

302 in Adélie Land (Riaux-Gobin *et al.*, 2011).

303

304 Although a large proportion of organic matter produced in the surface water is recycled in the upper

305 water column, the small fraction which is deposited in the sediment reaches the sea floor through large

306 particles sinking from above as "marine snow". This export production includes large algal cells, fecal

307 pellets, zooplankton carcasses and molts, and amorphous aggregates (Mayer, 1993). In the Ross Sea,

308   aggregates of *P. antarctica*, have been observed to sink at speeds of more than 200 m day^{-1}, meaning

309   they could reach deep water very quickly (Asper and Smith, 1999). In this way, a proportion of the lipid

310   content of *P. antarctica* and other algae is transported and sequestered in the sediments.

311

312   Initial diagenesis is characterized by the preferential degradation of more labile organic compounds e.g.

313   sugars, proteins, amino acids. Proportionally, lipids are relatively recalcitrant compared to other

314   compounds (e.g. amino acids, proteins) and thus are more likely to be preserved as molecular

315   biomarkers on geological timescales, even where the rest of the organism may be completely degraded

316   (Peters and Moldowan, 1993). The final proportion of lipids that are preserved within sediments are

317   affected by factors including the export production, O_2 content, residence time in the water column and

318   at the sediment/water interface before deposition, molecular reactivity, formation of macromolecular

319   complexes, adsorption to mineral surfaces and bioturbation (Meyers and Ishiwatari, 1993; Killops and

320   Killops, 2004). Within lacustrine sediments, a significant shift in FA distributions has been shown to

321   occur within 100 years due to early diagenesis, after which the FA distribution remains relatively

322   unaffected by diagenesis (Matsuda, 1978), thus major changes are assumed to reflect primary

323   environmental signals on longer timescales such as in our Holocene record. Due to the

324   hyperproductivity of the surface waters offshore Adélie land, we assume the dominant inputs of the C_{18}

325   FA are from algal sources in overlying waters and upcurrent regions. Allochthonous inputs e.g. long-

326   range aeolian transport of plant material are assumed to be minimal.

327

328   **4.2.2. Interpretation of hydrogen isotopes**

329   Compound-specific H isotopes of algal biomarkers are a well-used climate proxy in sediments

330   throughout the Cenozoic (e.g. Pagani *et al.*, 2006; Feakins *et al.*, 2012). Although diagenetic alteration,

331   including H-exchange, is possible within sedimentary archives, this has shown to be minimal in

332   sediments younger than 20 Ma (Sessions *et al.*, 2004). Furthermore, if H-exchange had occurred, we

333   would expect δ^2H values between different FA chain lengths and closely spaced samples to be driven

334   towards homogeneity, yet large variability remains, suggesting this is not the case. Thus, we are

335   confident that our measured H isotopes are indicating a primary signal throughout the Holocene.

336

The δ^2H value preserved in biomarkers is known to be correlated, but offset, with the δ^2H of the water from which the hydrogen was derived. Measured δ^2H can therefore be described as a function of either the δ^2H of the water source, or the fractionation occurring between source water and the lipid ($\varepsilon_{l/w}$) (i.e. vital effects), in which various environmental factors play a part (Sachse *et al.*, 2012).

The main environmental factors controlling $\varepsilon_{l/w}$ are salinity and temperature, with which δ^2H increases by 1-4‰ per increase in practical salinity unit (psu) (Schouten *et al.*, 2006; Sachse *et al.*, 2012) and decreases by 2-4‰ per degree C increase (Zhang *et al.*, 2009), respectively. The δ^2H_{FA} record from Site U1357 displays an absolute range of ca. 123‰, and millennial to centennial scale variability with an amplitude of ca. 50‰, throughout the core. This would imply extremely large and pervasive variations in temperature (up to ca. 60°C) and salinity (up to 123 psu) if fractionation driven by either of these factors were the main control. One study has shown the salinity of present day Adélie shelf waters to vary between 34 and 34.8 psu (Bindoff *et al.*, 2000), while tetraether-lipid based subsurface (50-200 m) temperature estimates from nearby Site MD03-2601 (about 50 km west of Site U1357) range from -0.17 to 5.35°C over the Holocene (Kim *et al.*, 2010). Therefore, fractionation changes driven by temperature or salinity cannot be invoked as a major control on δ^2H_{FA} in the Holocene.

Thus, the most parsimonious explanation relates to changes in δ^2H_{FA} of the water source (Sachse *et al.*, 2012). In the Adélie Basin, the most apparent controls on this are advection, upwelling or inputs of isotopically depleted glacial meltwater. The δ^2H_{FA} value within Antarctic glaciers is highly depleted relative to sea water due to the Rayleigh distillation process, leading to highly negative isotope values for precipitation over the continent.

The glacial meltwater originating from the Ross Ice Shelf is likely to combine ice precipitated throughout the Holocene and glacial period, and from both the East and West Antarctic Ice Sheets. However, as noted by Shackleton and Kennett (1975) in their first oxygen isotope record of the Cenozoic (see their Fig. 6), most of the ice that melts around the margin has been coastally precipitated (due to higher accumulation rates). Since ice precipitated further inland has a greater residence time (Shackleton and Kennett, 1975) and significantly lower accumulation rates it will contribute significantly less to this signal. Thus, the ice that was melting along this margin is best represented by average values of coastal ice dome records at a similar latitude to that which melted since the LGM

368   (such as TALDICE and Siple Dome) than more southerly locations. Glacial to Holocene δ^2H_{FA} values

369   from TALDICE, located on the western edge of the Ross Sea in the East Antarctic, for example, vary

370   between -276.2 and -330.3‰ (Steig *et al.*, 1998) (converted from $\delta^{18}O$ values following the global

371   meteoric water line (GMWL): $\delta^2H_{FA} = 8.13 (\delta^{18}O) + 10.8$), while values from Siple Dome on the

372   eastern edge of the Ross Sea in the West Antarctic, vary from ca. -200 to -293‰ (Brook *et al.*, 2005).

373   Taking the average of these values as a rough estimate for the meltwater gives a δ^2H value of ca. -

374   275‰. We note our calculations are based on averages of set time periods, which we expect would

375   integrate ice of various ages - rather than extreme values which could relate to specific melt events of ice

376   or biases to certain ages/regions. This seems reasonable - the isotopic signal of coastal surface waters

377   masses advected from the RIS to the Adélie land (as illustrated in Fig. 3 and 4) must integrate a range of

378   source areas across the RIS and from the coast around to Adélie Land.

379

380   In comparison to the highly negative glacial ice isotope composition, sea surface water $\delta^{18}O$

381   measurements taken near the Mertz Glacier offshore Adélie Land (140-150°E) in summer 2000-2001

382   ranged between -0.47 and 0.05‰ (Jacobs *et al.*, 2004), equivalent to δ^2H values of 6.9 to 11.2‰

383   (average = 9‰) following the GMWL. Thus, the two major hydrogen source pools (RIS glacial ice and

384   ocean water) have highly contrasting isotope values, meaning inputs of upstream glacial ice could have a

385   large effect on surface water δ^2H values in the Adélie Land region.

386

387   Taking the average glacial meltwater δ^2H value as -275‰ and the average modern Adélie surface water

388   δ^2H value of 9‰ as end-members, and assuming a biosynthetic offset between the FA and sea water of

389   173‰ (see below), we can use a simple mixing model to estimate the percentage of glacial meltwater

390   required in the surface waters to change the δ^2H_{FA} value to those recorded in U1357B samples. The

391   most negative values occur during the early Holocene, 11.4 – 8.2 ka, averaging -214.2‰ (n=18) which,

392   converted to a surface water value of -41‰, requires 17.6% of the surface water to be comprised of

393   glacial meltwater. During this time, we argue that large volumes of meltwater were reaching the core

394   site as local glaciers retreated, leading to intense surface-water stratification. Thus, a relatively high

395   percentage of meltwater in the Adélie Land surface waters seems reasonable. During the mid-Holocene

396   (5-4 ka), the average δ^2H_{FA} is very similar (-213.9‰, n=7), requiring 17.2% of the surface water to be

397   derived from glacial meltwater. During this time, we argue for the dominant meltwater source as coming

398   from the Ross Sea, and interpret this as a major period of glacial retreat (see section 5.2), during which

399   large volumes of meltwater are injected into the surface water and transported to the Adélie coast. In

400   contrast, the most recent samples (last 0.5 ka, n=7), which includes the most positive value of the record,

401   has an average δ^2H_{FA} value of -174.5‰. This brings the surface water value up to -1.5‰, which

402   approaches modern measured values, and requires just 3.7% (e.g. well within uncertainties) of the

403   surface waters in the Adélie Land to be glacial meltwater. However, it is also possible that the meltwater

404   was dominated by more LGM-aged ice. In either case, perturbation of the exact isotopic values still

405   indicate only significant changes in the flux of glacial meltwater can account for this signal. For

406   example, the use of -330‰ (LGM values) for the ice input gives an estimate of 3% of the surface water

407   being comprised of glacial meltwater for latest Holocene values, and 14.7% for pre 8 ka values. Taking -

408   240‰ (Holocene values) for the ice input gives an estimate of 4% for latest Holocene values, and 20%

409   for pre 8 ka values). Thus even with changing isotopic values though the deglacial, this signal of

410   changing meltwater flux would still dominate. We note these are semi-quantitative estimates, as the

411   salinity and temperature fractionation could reduce these estimates further (but cannot account for the

412   whole signal).

413

414   Surface water $\delta^{18}O$ values around Antarctica (below 60°S), measured between 1964 and 2006, ranged

415   from -8.52‰ to 0.42‰ (Schmidt *et al.*, 1999), the most negative value having been measured proximal

416   to the George VI Ice Shelf edge, where high melt rates have been observed (Potter and Paren, 1985). If

417   converted to δ^2H using the global meteoric water line, these values give a δ^2H range of 83.4‰. Thus,

418   our absolute δ^2H_{FA} range of 123‰ over the Holocene suggests a range of isotopically depleted

419   meltwater inputs to our core site over this time that are 1.5 times greater than that occurring in different

420   locations around the Antarctic in recent decades. This seems plausible based on geological evidence that

421   indicates large glacial retreat and ice mass loss occurred from the Ross Sea sector during the Holocene

422   (Anderson et al., 2014; McKay *et al.*, 2016; Spector et al., 2017), meaning resultant changes in surface

423   water are likely to be greater in magnitude than observed around the Antarctic in recent decades. This

424   assumes a relatively constant value for the isotopic composition of glacial meltwater, however, there is

425   likely to be some variability due to the possibility of melting ice of different δ^2H values. But, as

426   discussed above, the meltwater is best represented by the average values of the ice sheet, rather than

427   extreme values, since it must (over the broad expanse of the RIS) include an integrated signal, and thus

428   the actual variation in meltwater δ^2H will be significantly within the range of the end-members.

429

430   Although the biosynthetic fractionation of the C_{18} FAs in U1357B is unknown, we assume that the offset

431   with surface water remains relatively constant throughout the record. Sessions *et al.* (1999) showed the

432   biosynthetic fractionation of hydrogen isotopes in the C_{18} FA from four different marine algae to range

433   from -189 to -157‰. If we take the average of these values of 173‰ and apply this as a biosynthetic

434   offset to the youngest samples in U1357B (last 0.5 ka, n=7), which includes the most positive value of

435   the record, gives an average δ^2H_{FA} value of -174.5‰. This brings the surface water value up to -1.5‰,

436   which approaches modern measured values (Jacobs *et al.*, 2004).

437

438   Furthermore, it is interesting to note that the biosynthetic offsets measured by Sessions *et al.* (1999) for

439   the C_{18} FA from different algal species have a total δ^2H range of 32‰. Although we cannot dismiss

440   changes in the relative contribution of C_{18} from different species in U1357B samples (and thus different

441   biosynthetic fractionations), we argue this would only be a minor control on δ^2H compared to other

442   influences. As a thought experiment, taking the above end-members for biosynthetic fractionation from

443   Sessions *et al.* (1999), even with a 100% change in C_{18} producer to a different algal source, this could

444   only explain a quarter of the observed δ^2H change (i.e. 32‰ of 123‰).

445

446   Therefore, we interpret the first order control on δ^2H_{FA} at Site U1357 as inputs of isotopically depleted

447   glacial meltwater. Such inputs are, in turn, influenced by the mass balance of the proximal or up-current

448   glaciers and ice-shelves.

449

450   4.3 Other proxies

451   Grain size, natural gamma radiation (NGR) and terrigenous and biosiliceous mass accumulation rates

452   (MARs) reflect changing sediment delivery either driven via local glacial meltwater discharge or

453   advection of suspended sediment by oceanic currents. The diene/triene HBI ratio is used as a proxy for

454   coastal sea ice presence (Massé *et al.*, 2011), in which high values indicate greater sea ice extent over

455   the core site. The HBI diene, also known as Ice Proxy for the Southern Ocean with 25 carbon atoms

456   (IPSO25), has been shown to derive from a sea-ice associated diatom (Belt et al., 2016), whereas the

457   HBI triene is produced in the marginal ice zone (Smik et al., 2016). Ba/Ti enrichment is considered to

458   reflect enhanced primary productivity. Interpretation of these proxies is discussed in more detail in

459   Supplementary Information S2.

460 **5 RESULTS**

461 **5.1. Model simulations**

462 We employed a series of sensitivity tests from a high-resolution numerical ocean model by releasing a

463 range of meltwater volumes (0.01 to 1 Sv) from along the front of the Ross Ice Shelf (RIS) to determine

464 its pathway. This demonstrates that, even under the lowest flux scenarios, freshwater is transported

465 anticlockwise, entrained within the coastal current (Fig. 2 and 3), and reaches Site U1357 within a year.

466 Moreover, although the higher input scenarios are not realistic values for the release of meltwater since

467 the LGM, the full range of simulations show a strong linear relationship between meltwater flux and

468 salinity change at the core site (Fig 3), suggesting the magnitude of the signal recorded at Site U1357 is

469 directly related to the magnitude of meltwater released. Thus, we argue that any changes in Ross Sea

470 water mass properties (salinity and temperature) would have a direct influence on surface water mass

471 properties at Site U1357 during the Holocene.

472 **5.2 Geochemical data**

473

474 The main datasets from Core U1357 are displayed in Fig (2) and S2. FA δ^2H (Fig 4a) shows and overall

475 trend towards more positive values over the course of the Holocene, indicating a decline in glacial

476 meltwater input. There is a notable deviation from this trend in the mid-Holocene involving a sustained

477 period of more negative δ^2H values, suggesting a peak in meltwater input, centred on ca. 4.4 ka. This

478 mid-Holocene deviation in FA δ^2H coincides with an increase in the HBI diene/triene ratio (Fig. 4c),

479 indicating a baseline shift in sea ice conditions whereby greater sea ice concentrations are sustained for

480 the rest of the Holocene. This is a similar pattern to the relative abundance of the *Fragilariopsis curta*

481 group (Fig 4b), a sea ice diatom group in core MD03-2601 also indicating a shift in sea ice

482 concentrations. Along the entire record, Ba/Ti ratios show persistent periodic fluctuations in marine

483 productivity, with values between 0.1 and 2.7 (Fig. 4g). A marked enrichment can be observed at ca. 4.4

484 ka reaching Ba/Ti ratio values over 36.1, suggesting a peak in primary productivity, before declining to

485 background levels again (Fig. 4g).

486

487 **5.3 Sedimentological data**

488   The stratigraphy of U1357B is divided into three units: the lowermost 10 cm recovered Last Glacial

489   Maximum (LGM) till (Unit III), overlain by 15 m of laminated mud-rich diatom oozes with ice rafted

490   debris (IRD) (Unit II), and the upper most 171 m (Unit I) consists of laminated diatom ooze with a

491   general lack of IRD and a significant reduction in terrigenous sediment (Escutia *et al.*, 2011).

492   Between ca. 11.4 and 8 ka, U1357B has a relatively high terrigenous component (i.e. high Natural Gamma

493   Radiation (NGR) content and low BSi%; Fig S4). The grain size distribution contains coarse tails of fine

494   (125-250 μm) to medium sands (250-500 μm), but only one sample contains coarse sands (>500 μm) that

495   may represent ice-berg rafted debris (IBRD). However, terrigenous content and IBRD is more common in

496   the underlying Unit II. The fine-grained sands and muds have a distribution with similar modes to overlying

497   intervals, albeit with an increase in the size of the coarse silt and very fine sand modes. There is a subtle

498   increase in sorting up core between ca. 11.4 and ca.8 ka (from very poorly to poorly sorted, Fig. 5c).

499   Between 9 and 4.5 ka, mass accumulation rates (MARs) (both biogenic and terrigenous; Fig. 5e) are

500   relatively high, albeit with millennial scale variability. However, the mean grain size and sorting of the

501   terrigenous material is relatively stable throughout the entire interval, and as with the rest of Unit I there

502   is an almost complete lack of IBRD. There is a rapid increase in mud content at 4.5 ka coincident with a

503   reduction in both the biogenic and terrigenous MARs, although the terrigenous MAR curve shows higher

504   accumulation rates than the biogenic MAR curve (Fig. 5e and f).

505

506   **6. DISCUSSION**

507
508   The sedimentology and geometry of the drift prior to ~11.4 ka (Unit II) is consistent with the calving

509   bay reentrant model (Domack *et al.*, 2006; Leventer *et al.*, 2006) (Fig. 1 and Supplementary Fig. S4;

510   Supplementary Materials), whereby LGM ice retreated in the deeper troughs while remaining grounded

511   on shallower banks and ridges. Sediment laden meltwater and IRD content in Unit II (>11.4 ka) is thus

512   likely derived from local outlet glaciers. However, anomalously old radiocarbon ages due to glacial

513   reworking precludes development of a reliable age model prior to the Holocene (Supplementary

514   Materials).

515   The results of model simulations (Section 5.1) indicate that, although several small glaciers within

516   Adélie Land may contribute meltwater to the site, the region is also likely to be influenced significantly

517   by changes in Ross Sea waters. Freshwater release simulations from the Ross Ice Shelf (RIS) confirm

518   this oceanographic continuity between the Ross Sea and the Wilkes region (Fig. 2). All five simulations

519   indicate that meltwater released from the edge of the RIS is almost completely entrained within the

520   westward coastal surface current and reaches Site U1357 within 4 months to 1 year (Fig 3). These fluxes

521   cover a wide range of meltwater inputs and show a strong linear relationship with salinity at the core site

522   (Fig. 4a). This suggests that the magnitude of the signal recorded at Site U1357 is directly related to the

523   magnitude of the meltwater input.

524   Local processes do also play a critical role in this region. For example, episodic calving events of the

525   Mertz Glacier tongue release fast ice over the drill site and create strong surface water stratification,

526   cutting off local AABW production (Campagne *et al.*, 2015). Although appearing to be only a local

527   process, there is still a regional (Ross Sea) influence, as this fast ice that builds up behind the Mertz

528   Glacier is formed by the freezing of fresher AASW transported from the Ross Sea (Fig 2). Thus,

529   conditions in the Ross Sea, such as the melting of isotopically depleted glacial ice, would influence both

530   the isotopic composition and amount of this sea ice.

531

532   **6.1 Early Holocene**

533   The base of the drift deposit shows downlapping of material suggesting a supply from the south,

534   indicating local focusing of meltwater and terrigenous material was the dominating influence until 11.4

535   ka (Supplementary Materials S2.2 and Fig. S4). This is overlain by onlapping strata (Unit I) with the

536   drift forming an east-west elongation on the northern flank of the Dumont d'Urville Trough, which is

537   more consistent with advection of material from the east than with delivery from local outlet glaciers to

538   the south. Thus, an increased meltwater influence from the Ross Sea is likely since this time.

539

540   Due to the potential for competing sources of glacial meltwater in the earliest Holocene, we focus our

541   study on Unit I, where there is less influence of calving bay processes (Escutia *et al.*, 2011). However,

542   the earliest part of Unit I (11.4 to 8 ka BP), which includes the most negative δ^2H_{FA} values, is

543   characterized by a very gradual upcore increase of sorting in the terrigenous sediment supply,

544   decreasing natural gamma ray (NGR) values (Fig. 5b and c) and a general lack of IRD (Escutia et al.,

545   2011). We conservatively interpret this as potentially maintaining some local glacial meltwater input

546   from local outlet glaciers in the lowermost interval of Unit I. Nevertheless, this process was probably

547   greatly reduced relative to Unit II deposition and it is likely much of this signal between 11.4 and 8 ka

548   could still be derived from water masses advecting to the site from the east (e.g. the Ross Sea).

549

550   This is supported by geological and cosmogenic evidence which demonstrates that the majority of the

551   margin of the East Antarctic, and also the Amundsen Sea margins, had retreated to their modern-day

552   positions by ~10 ka (Bentley et al., 2014; Mackintosh et al., 2014; Hillenbrand et al., 2017). Thus, these

553   margins are unlikely to contribute large scale shifts in meltwater fluxes to the Adélie Coast during most

554   of the Holocene. The history of grounding line retreat in the Ross sea is relatively well-constrained,

555   particularly in the Western Ross Sea, and the loss of residual ice caps appears to be largely complete by

556   ca. 7 ka to the immediate north of Ross Island, near present day calving line front of the Ross Ice Shelf

557   (Anderson et al., 2014; McKay et al. 2016). Indeed, the phase of isotopically depleted glacial meltwater

558   is apparent at Site U1357 between 8 and 7 ka could be sourced from the Ross Sea, reconciling our data

559   with these chronologies. Prior to 8 ka, any meltwater signal in U1357B is potentially influenced by local

560   glacier retreat, based on the caveats noted earlier in the grainsize and geophysical datasets (S2.2),

561   although we note a dominant Ross Sea contribution to this signal is possible.

562

563   Glacial retreat, however, persisted in the Ross Sea until at least 3 ka (Anderson et al., 2014; Spector et

564   al., 2017) providing a large upstream source of meltwater feeding into the Adélie Coast. We therefore

565   interpret our meltwater signal as being dominated by Ross Sea inputs since at least 8 ka, but potentially

566   as early as 11.4 ka. Furthermore, the retreat of grounded ice from the outer Ross Sea continental shelf

567   was accompanied by the growth of a significant floating ice shelf (which was not the case in the

568   Amundsen Sea or proximal East Antarctic coast) (Bentley et al., 2014).

569

570   An overall trend to more positive δ^2H_{FA} values, from the most negative value of the record at ~9.6 ka, to

571   ~8 ka indicates decreasing meltwater (Fig. 4a), thus suggesting a gradually diminished input from either

572   local outlet glaciers or the Ross Sea. This is associated with an increase in MARs, between 10 and 8 ka,

573   and is tentatively interpreted to represent the final retreat of residual ice from local bathymetric highs

574   allowing more material to advect into the drift (Fig. 5e). Although there is millennial scale variability,

575   MARs remain relatively high until 4.5 ka. However, δ^2H_{FA} and MARs show greater coherence at the

576   millennial-scale after 7 ka BP, suggesting that increased fluxes of glacial meltwater broadly

577 corresponded to stronger easterly currents, which advected biogenic and terrigenous material into the

578 drift.

579

6.2 Middle Holocene

581 A negative excursion in δ^2H_{FA} starting from 6 ka and culminating at 4.5 ka is interpreted to record a

582 period of enhanced glacial meltwater flux to the site relating to a final retreat phase of the major ice

583 sheet grounding line in the Ross Sea embayment (Fig. 6). A marked enrichment of Ba/Ti ratios also

584 occurs at 4.5 ka, reaching values of 36.1, on a background of baseline fluctuations between 0.1 and 2.7

585 (Fig. 2g), which suggests enhanced primary productivity, potentially driven by meltwater-induced

586 stratification. Ongoing Holocene retreat in the Ross Sea is interpreted to be primarily the consequence of

587 marine ice sheet instability processes resulting from the overdeepened continental shelf in that sector

588 (McKay et al., 2016). We use the model presented by Lowry et al., (2019) to help constrain the pattern

589 and rate of retreat of the grounding line to the south of Ross Island. This model compares geological

590 data with ice sheet model experiments that were forced by a range of environmental conditions. These

591 experiments indicate that the Ross Ice shelf cavity only started to expand once the grounding line

592 retreated to the south of Ross Island. Furthermore, to reconcile these model experiment with geological

593 datasets, the cavity expansion was not completed until the mid-Holocene (ca. 5 ka). This reconciles well

594 with [10]Be exposure ages of erratics in coastal nunataks at the confluence of the Mercer Ice Stream and

595 Reedy Glacier indicate 105 m of ice sheet deflation since 6.8 ka, with 40 m of this after 4.9 ka (Todd et

596 al., 2010), indicating the most rapid phase of retreat occurred between 6.8 ka and 4.9 ka. More recent

597 deflation profiles for the Beardmore Glacier (84°S) and Scott Glacier (86°S) regions show sustained

598 thinning between ca. 9 and 8 ka, but the Scott Glacier experience a second phase of rapid thinning of ca.

599 200 m between 6.8 and 5.3 ka (Fig. 2h), followed by a slower rate of thinning of between 5.3 and 3.5 ka

600 of ca. 100 m. Ages younger than this, near the modern surface are thought to be related to surface

601 ablation rather than dynamic thinning. This suggests that the grounding line was at its modern location

602 by ca. 3.5 ka (Spector et al., 2017) although it may have potentially retreated further south, followed by

603 a short duration readvance of the grounding line (Kingslake, et al., 2018). Glaciological evidence from

604 radar profiles suggests the development of divide flow on Roosevelt Island occurred sometime between

605 3 and 4 ka BP, suggesting that the ice sheet thickness was at least 500 m thicker until this time (Conway

606 et al., 1999). Combined, these lines of evidence suggest the majority of grounding line retreat south of

607 Ross Island occurred after 8 ka, with a sustained retreat occurring after 6.8 ka, consistent with the timing

608   of the largest inputs of glacial meltwater feeding the U1357 site. However, a younger age (e.g. 3 – 3.5

609   ka) for final establishment of the modern grounding line position is consistent with our interpretation, as

610   although the meltwater signal in δ^2H_{FA} peaks at 4.5 ka, it does not stabilise at lower levels until 3 ka.

611

612   The δ^2H_{FA} peak at 4.5 ka in U1357 coincides directly with a rapid shift in HBI biomarker ratios at the

613   site (Fig 4a and c), as well as sea ice proxies recorded in nearby site MD03-2601 (Fig. 4b), in the Ross

614   embayment (Taylor Dome ice core on a revised age model) (Steig *et al.*, 1998; Baggenstos *et al.*, 2018)

615   (Fig. 4d) and other sectors of the East Antarctic margin in Prydz Bay (JPC24) (Denis *et al.*, 2010) (Fig.

616   4e), reflecting a widespread increase in coastal sea-ice concentration and duration. We interpret

617   decreasing MAR and finer-grained terrigenous content (e.g. increased mud percent) at Site U1357 after

618   4.5 ka (Fig. 5e and f) to also be a consequence of increased coastal sea ice, reducing wind stress on the

619   ocean surface and limiting the easterly advection of detritus to the drift deposit.

620

621   Coastal sea-ice concentration and duration remain high throughout the rest of the Holocene as recorded

622   by our HBI data (Fig. 4c); sea ice diatoms in core MD03-2601 (Crosta *et al.*, 2008); methanesulfonic

623   acid concentration in Taylor dome ice core(Steig *et al.*, 1998); and sea ice diatoms in core JPC24 (Denis

624   *et al.*, 2010), compared to the period before 4.5 ka, despite a decrease in glacial meltwater flux to the

625   U1357 site. In addition, meltwater input prior to 4.5 ka does not have a major influence on sea ice

626   extent. Thus, an increase in meltwater flux cannot explain the Neoglacial intensification of sea ice at

627   ~4.5 ka. Here, we propose that greater coastal sea ice cover since 4.5 ka is related to the development of

628   a large ice-shelf cavity in the Ross Sea as the ice sheet retreats (Fig. 6), which pervasively modified ice

629   shelf-ocean interactions and increased sea ice production. Models suggest a large cavity on the

630   continental shelf increases contact between basal-ice and circulating ocean water, driving the formation

631   of a cool, fresh water mass feeding into the AASW, stabilizing the water column and enhancing the

632   production of sea ice (Hellmer, 2004) (Fig. 6). However, under small cavities such as in the modern

633   Amundsen Sea influenced by warm-water incursions, ice shelf melting results in an "ice pump"

634   enhancement of sub-ice shelf circulation. This increases flow of warm Circumpolar Deep Water (CDW)

635   under the ice shelf that is 100-500 times the rate of melt, and this volume of water does not allow for

636   supercooling. Small cavity ice shelf outflows are therefore warm and act to restrict sea ice at the ice

637   shelf front (Jourdain *et al.*, 2017). Thus, during the Holocene, the size of the cavity must have reached a

638   threshold after which this positive warming feedback switched to a negative feedback. We argue that

such a tipping point takes place at 4.5 ka BP, when our proxy data suggest meltwater peaks, and would explain why the increase in sea-ice concentration appears rapid and only occurs at the peak of the meltwater input, and not during its prior increase, or previous meltwater inputs (Fig. 4a-g).

Although the glacial meltwater volume is greatly reduced after 4.5 ka BP, the volume of Ice Shelf Water (ISW) produced beneath the modern RIS is estimated at 0.86 Sv-1.6 Sv (Holland *et al.*, 2003; Smethie and Jacobs, 2005). We note that ISW is not glacial meltwater, but it is defined as a supercooled water mass formed through interaction with the base of the RIS, but once formed acts to modify other water masses in the Ross Sea. A significant proportion of ISW is high salinity and is thus advected northwards at intermediate waters depth to ultimately form AABW. However, a significant volume of ISW is lower salinity and buoyant, due to development of frazil ice, and acts to mixes with surface waters (Robinson *et al.*, 2014). Currently, a 0.4 Sv plume of ISW in the western margin of the Ross Ice Shelf (Robinson *et al.*, 2014) is directly delivered to the surface resulting in enhanced sea ice production, while seasonal melt of this enhanced sea ice further acts to cool and freshen surface waters. Although unrealistic in the context of a post-LGM meltwater flux from the Ross Sea alone, the larger meltwater release scenarios in our simulations (0.5 to 1 Sv) show the potential pathways that a cool, fresher surface water mass collecting and forming on the broad Ross Sea continental shelf would follow (Fig. 2b). These waters are transported in easterly coastal currents to the Weddell Sea and the Antarctic Peninsula. This eventually retroflects to join the Antarctic Circumpolar Current (Fig. 2b), and thus has potential for cooling and freshening in the South Atlantic far offshore, as the ice shelf cavity increased in the Ross Sea. Indeed, offshore site ODP 1094 records increased lithics in the South Atlantic after 4.5 ka (Fig. 4f), relative to the period before, suggested to have been predominantly transported by sea ice indicating a cooling in sea surface temperatures and increase in sea-ice extent in the South Atlantic at this time (Hodell et al., 2001; Nielsen *et al.*, 2007). However, it also is feasible that this circum-Antarctic cooling signal indicates similar melt processes may have been occurring in the Weddell Sea at ~4.5 ka, as suggested by cosmogenic nuclide data (Hein *et al.*, 2016).

6.3 What Drove the Neoglacial Transition?

Our observed coastal sea-ice increase is part of a widespread transition to Neoglacial conditions both globally and at high southern latitudes (Kim *et al.*, 2002; Masson-Delmotte *et al.*, 2011; Marcott *et al.*, 2013; Solomina *et al.*, 2015). However, most current climate models do not simulate this cooling trend,

Climate of The Past   Page **22** of **41**   Ashley et al., 2019

670   resulting in a significant data-model mismatch (Liu *et al.*, 2014) (Fig. 7). Marine ice sheet retreat along

671   the Pacific margin of West Antarctic has previously been proposed to be triggered by enhanced wind-

672   driven incursions of warm CDW onto the continental shelves in the early Holocene (Hillenbrand *et al.*,

673   2017), with continued retreat in the Ross Sea being the consequence of the overdeepened continental

674   shelf and marine ice sheet instability processes (McKay *et al.*, 2016). We propose that a series of

675   negative feedbacks was also associated with the latter phases of this retreat due to the RIS cavity

676   expansion that occurred in the mid-Holocene, with similar processes possibly occurring in the Weddell

677   Sea, leading to the onset and continuation of Neoglacial conditions. Widespread albedo changes

678   associated with increased coastal sea ice would have amplified regional cooling trends (Masson-

679   Delmotte *et al.*, 2011), whilst increased stratification resulting from seasonal sea-ice melt and increased

680   ISW production drove the deepening of the fresher water surface isopycnal at the continental shelf

681   break. Grounding line retreat creates new space for continental shelf water masses to form, while ice

682   shelf cavity expansion promotes supercooling of waters circulating beneath the ice shelf, and freshening

683   of AASW. Thus, as seasonal sea ice melt and ice shelf supercooling processes played a greater role in

684   enhancing AASW cooling and production on the continental shelf, they would have acted to restrict

685   warmer subsurface water transport onto the continental shelf (Smith Jr. *et al.*, 2012) (Fig. 6).

686   Furthermore, the Neoglacial sea-ice increase itself may have been associated with a stabilising feedback

687   mechanism (which also is not resolved in ice-ocean models) through its role in dampening ocean-

688   induced wave flexural stresses at ice shelf margins, reducing their vulnerability to catastrophic collapse

689   (Massom *et al.*, 2018). We suggest that some combination of the above processes could have acted to

690   slow the rate of Ross Sea grounding line retreat and reduced basal ice shelf melt as indicated by a trend

691   towards more positive $\delta^2 H_{FA}$ values in U1357 between 4.5 and 3 ka (Fig. 4a). Furthermore, large

692   Antarctic ice shelves currently have large zones of marine accreted ice resulting from supercooling

693   (Rignot *et al.*, 2013), thus the signature of $\delta^2 H_{FA}$ is anticipated to become more positive as the ice shelf

694   approaches a steady state of mass balance, relative to the thinning phases when basal melt rates exceed

695   that of accretion. The stabilization of $\delta^2 H_{FA}$ values observed at 3 ka in U1357 suggests the Ross Ice

696   Shelf has maintained a relatively steady state of mass balance since this time.

697

698   A recent study implies that the late Holocene shift in coastal versus open water sea ice patterns in the

699   Ross Sea was driven an increase in katabatic winds since at least 3.6 ka in the Ross Sea (Mezgec *et al.*,

700   2017), leading to enhanced polynya activity. During colder Antarctic climates, increased latitudinal

temperature gradients enhanced katabatic winds in the Ross Sea (Rhodes *et al.*, 2012). This is consistent with our hypothesis, as we interpret this katabatic wind and polynya activity signal to be a response to the preceding Neoglacial cooling at 4.5 ka and evolution of the modern ocean-ice shelf connectivity, which our data suggest was primarily driven by ice shelf cavity expansion. Furthermore, this transition takes place on the background of declining winter insolation (Berger and Loutre, 1991) which would have acted to further enhance and maintain these changes. This insolation decline has previously been hypothesised as a driver of the Neoglacial increase in coastal sea ice in both Prydz Bay and the Adélie Land regions (Denis *et al.*, 2010), however this monotonic decrease contrasts with the markedly rapid increase in sea ice observed in many records (Fig 2). Our mechanism of ice shelf cavity expansion, reaching a threshold that promoted significant supercooling of continental shelf water masses, reconciles both the rapidity and timing of Neoglacial onset in the middle Holocene.

7. Conclusions and Implications for Antarctic Climate, Sea-Ice and Ice Shelf Behaviour

Our multiproxy record of changing oceanographic conditions in the Adélie Land region indicates a significant meltwater event during the middle Holocene. Comparison of this record with pre-exisitng studies from around the Antarctic margin indicates this was likely associated with final phases of deglaciation of the Ross Sea embayment. Expansion of the Ross Ice Shelf cavity at this time is proposed to have led to modification of surface water masses formation processes on the continental shelves of Ross Sea and Adélie Land and contributed to widespread Antarctic surface water cooling and increased coastal sea ice during the late Holocene Neoglacial. The lack of these coupled ice-ocean processes is apparent in recent Earth system model experiments, in particular the incorporation of evolving ice shelf cavities, with Trace-21k for example, instead simulating a decrease in Antarctic sea-ice extent and thickness after 5 ka (Fig. 7). These model outputs are in direct contrast to multiple lines of proxy data in this study and previous work (Steig *et al.*, 1998; Crosta *et al.*, 2008; Denis *et al.*, 2010). Consequently, our results provide insights into the magnitude of this data-model mismatch, as well as a mechanism for rapid sea-ice change and grounding line stabilisation on the background of a warming climate (Liu *et al.*, 2014), both on modern and Holocene time scales. Better representation of the role of evolving ice shelf cavities on oceanic water mass evolution and sea-ice dynamics, which our data indicate acted as a strong negative feedback, will be fundamental to understanding the oceanographic and glaciological implications of future ice shelf loss in the Antarctic.
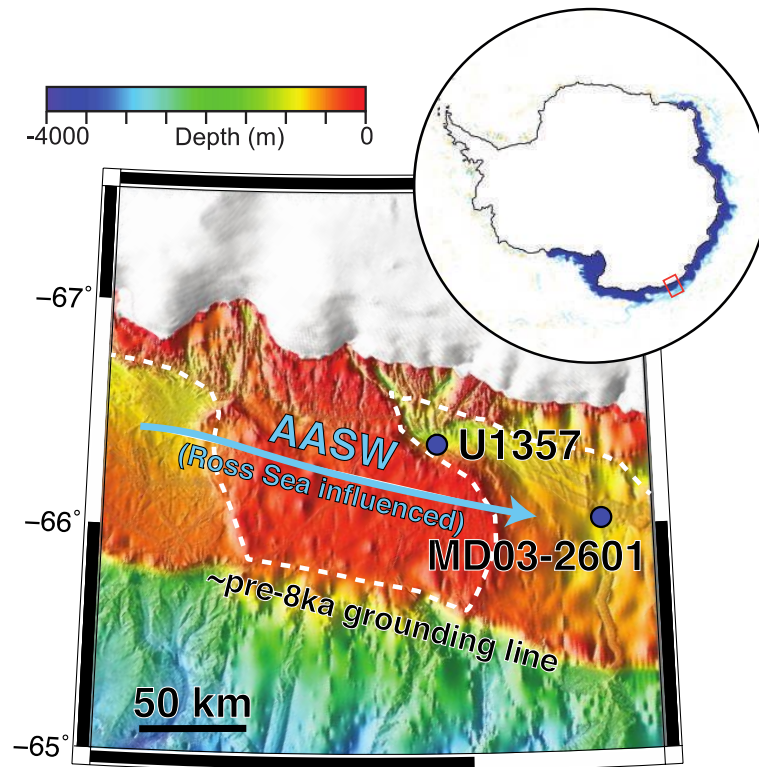
Figures

Figure 1: Location of Sites U1357 and MD03-2601 (blue dots). The ice sheet grounding line formed a calving-bay environment (dashed white line) prior to 11.4 ka, but since at least 8.2 ka Antarctic Surface Water flow is largely advected from the Ross Sea (blue line). Inset map: pathway of freshwater (dark blue) after 1 year of 1 Sv meltwater released from along the edge of the Ross Ice Shelf in a model simulation.
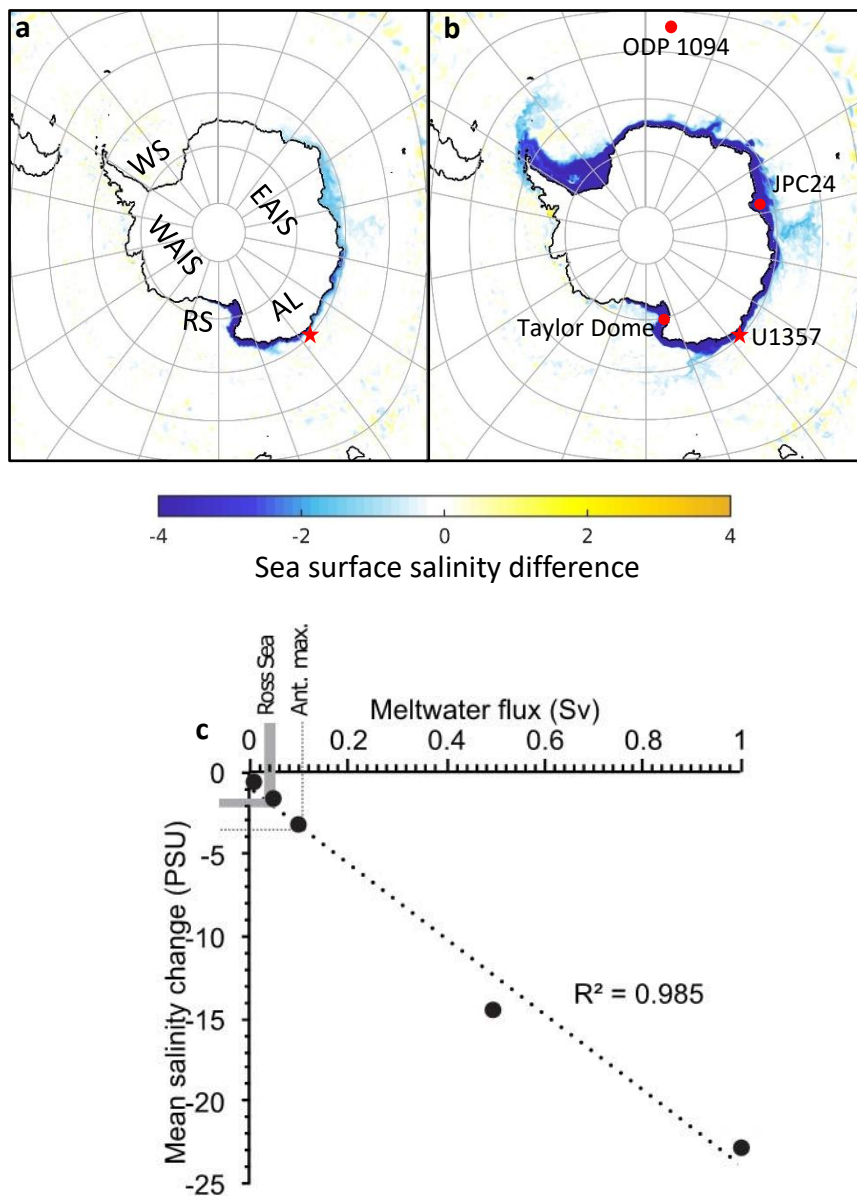
Figure 2: MITgcm simulations of meltwater release from along the edge of the Ross Ice Shelf. First

two images show sea-surface salinity difference (in practical salinity units) after 3.5 model years

resulting from meltwater release volumes of a) 0.1 Sv ($2x10^{13}$ m^3 total ice volume equivalent) and b) 0.5

Sv ($1x10^{14}$ m^3 total ice volume equivalent). Red star indicates position of Site U1357 (this study) and

red dots show positions of other core sites mentioned in this study where a Mid-Holocene increase in sea

ice and/or cooling is recorded: Taylor Dome (Steig *et al.*, 1998; Baggenstos *et al.*, 2018), JPC24 (Denis

et al., 2010) and ODP 1094 (Nielsen *et al.*, 2007). AL = Adélie Land, RS = Ross Sea, WS = Weddell

Sea, EAIS = East Antarctic Ice Sheet, WAIS = West Antarctic Ice Sheet. c) Scatter plot of simulated

meltwater flux (Sv) against mean salinity difference at U1357 core site. Grey band indicates range of

plausible Holocene to deglacial Ross Sea meltwater inputs. Dotted line indicates maximum Antarctic meltwater during the Holocene.
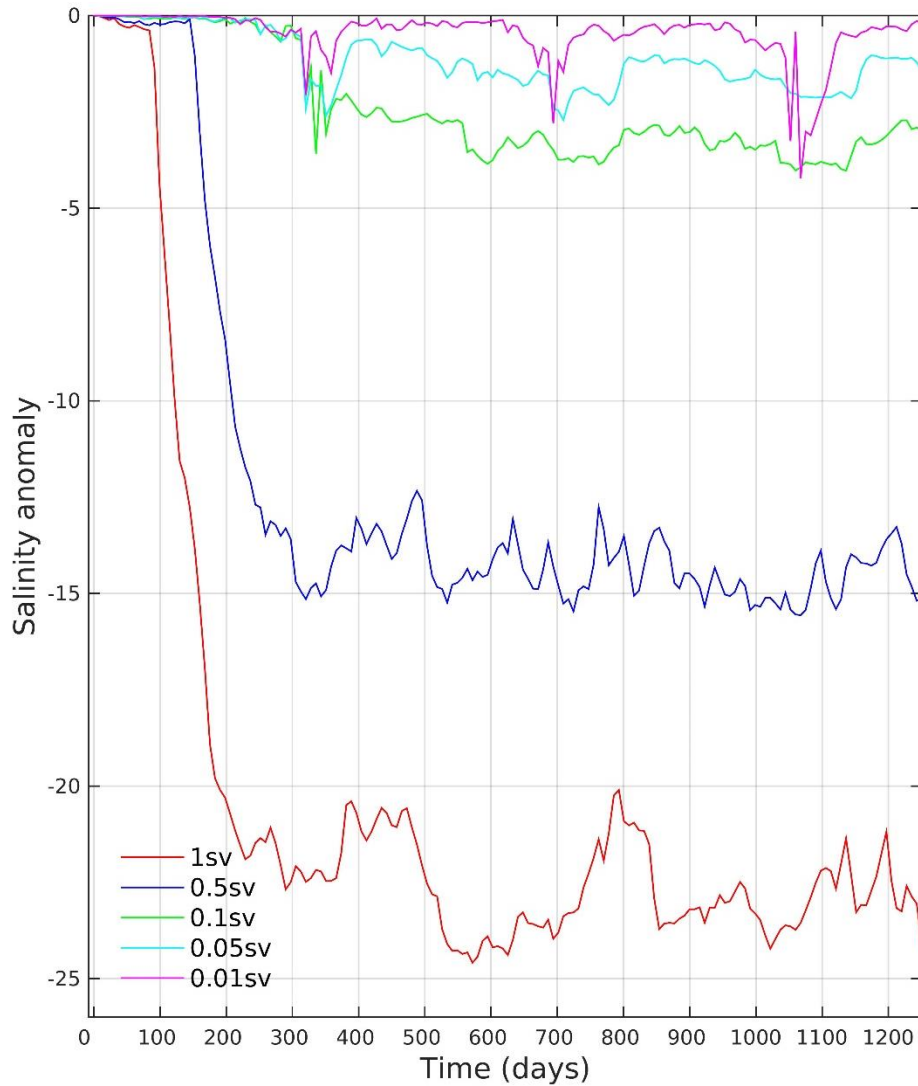
Figure 3 Simulated salinity anomalies over time at Site U1357 for the five meltwater release experiments.

789
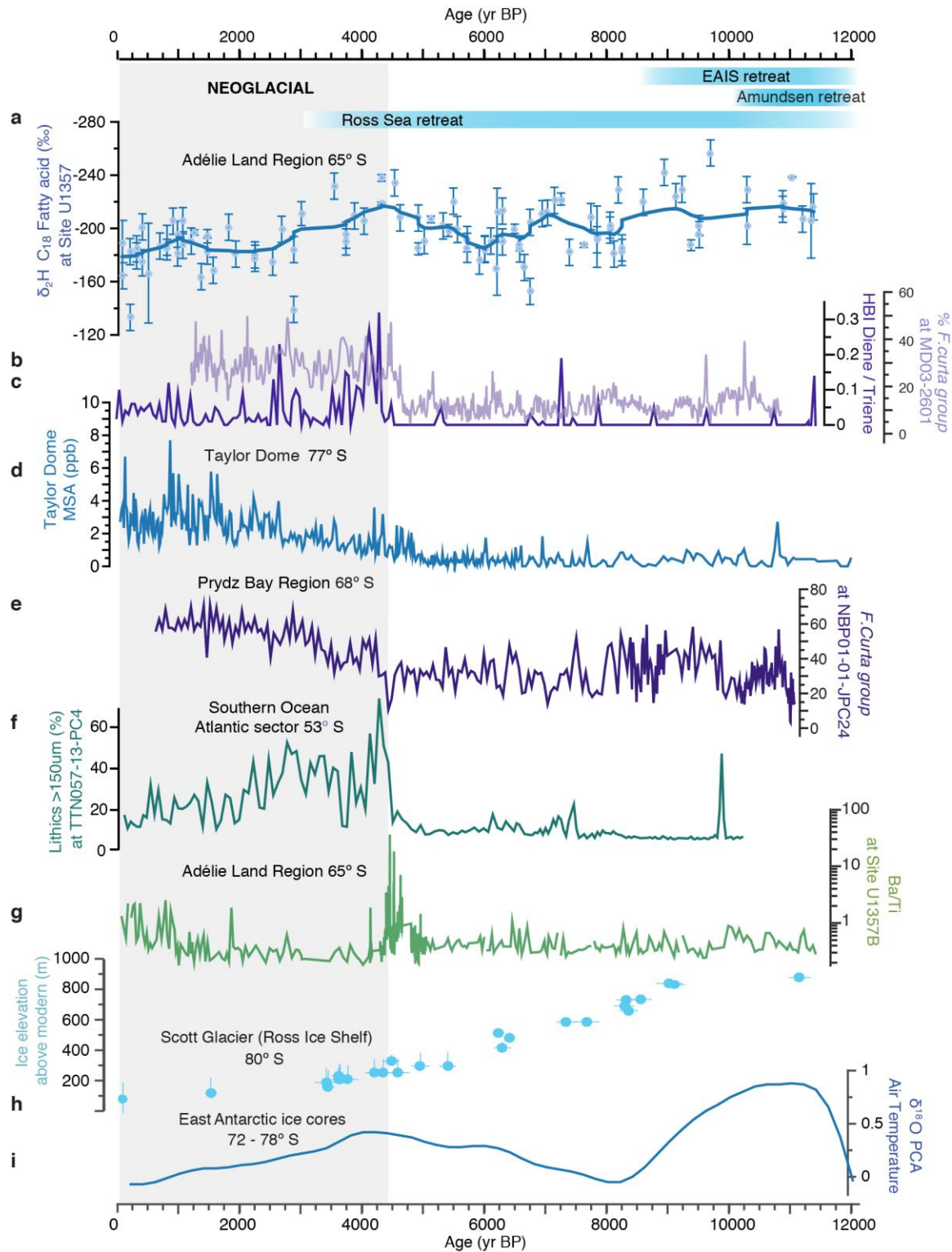
Figure 4: Holocene Adélie Land proxy records from IODP Site U1357 and other circum-Antarctic

sites. Glacial retreat chronologies are shown as bars at the top as discussed in the text. a) δ^2H C_{18} fatty

acid at Site U1357 (errors bars based on replicates), with robust locally weighted smoothing (rlowss). b)

793 *Fragilariopsis curta* group (*F. curta* and *F. cylindrus*) relative abundance at MD03-2601, as a proxy of

794 sea-ice conditions (Crosta *et al.*, 2008) c) di-unsaturated HBI ($C_{25:2}$; Diene)/tri-unsaturated HBI isomer

795 ($C_{25:3}$; Triene) ratio at Site U1357 d) Methanesulfonate (MSA) concentrations (ppb) from Taylor Dome

796 ice core e) *F. curta* group relative abundances in core NBP-01-JPC24 f) Coarse lithic (ice-rafted)

797 content at TTN057-13-PC4 (Hodell et al., 2001) g) Ba/Ti (logarithmic scale) at Site U1357 h) ^{10}Be

798 cosmogenic nuclide ages from Scott Glacier in the SW Ross Ice Shelf region (Spector *et al.*, 2017) i)

799 Temperature signal from principal component analyses of five δ^{18}O records in five East Antarctic ice

800 cores (Vostok, EPICA Dome C, EPICA Dronning Maud Land, Dome Fuji and Talos Dome) (Masson-

801 Delmotte *et al.*, 2011).

802

803

804

805

806

807

808

809

810

811

812

813

814

815

816

817

818

819

820

821

822

823

824

825

826

827

828
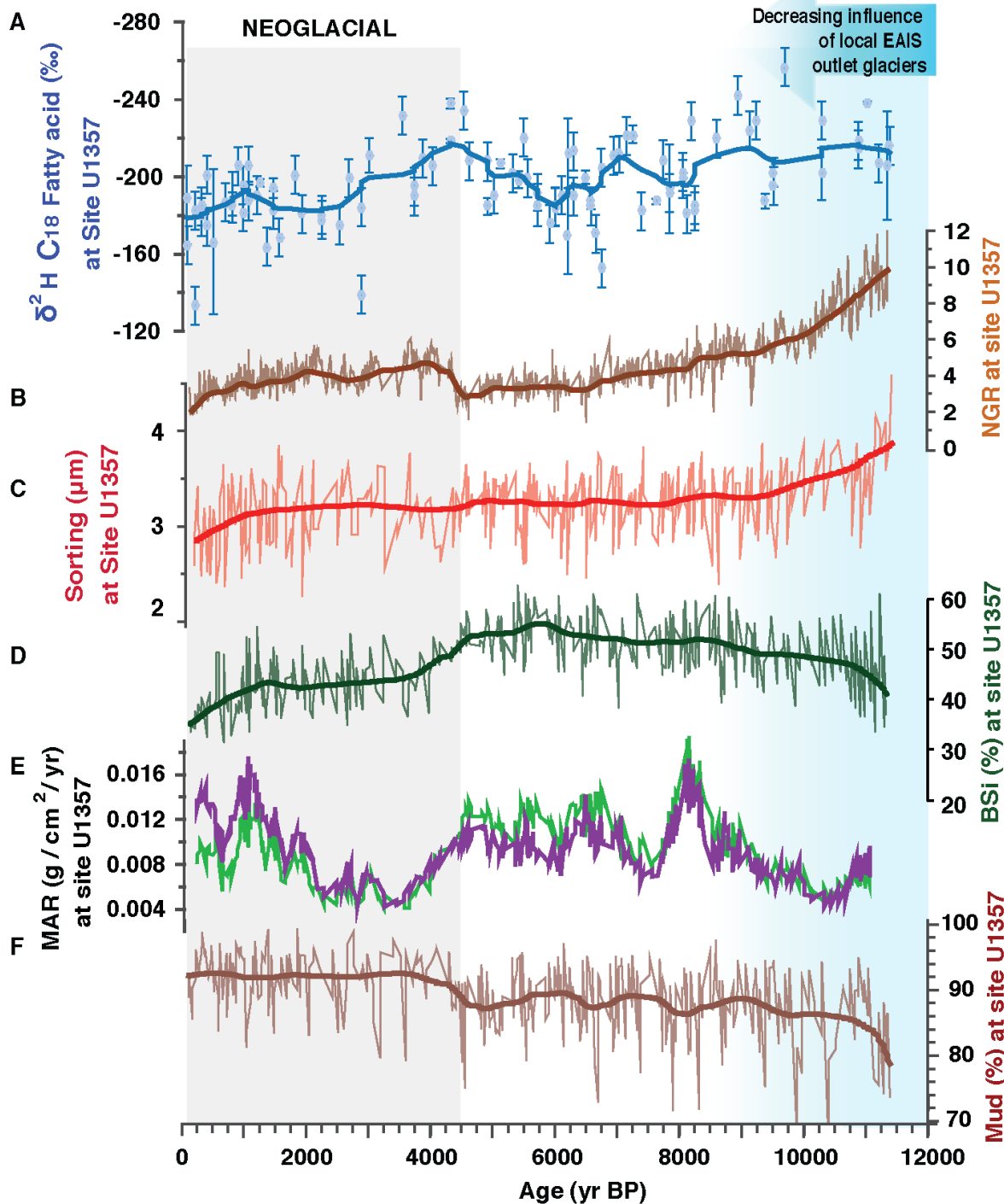
Figure 5 Holocene Adélie Land proxy records from IODP Site U1357 a) C_{18} fatty acid δ^2H (errors bars based on replicate analyses), heavy line is a robust locally weighted scatterplot smoothing (rlowss) b) Natural Gamma Radiation, heavy line is a rlowss c) grain sorting (μm) calculated following Folk and Ward (1957), heavy line is a rlowss d) Percentage of biogenic silica (BSi), heavy line is a rlowss; e) Mass accumulation rates of biogenic (green line) and terrigenous (purple line) material f) Percentage of mud, heavy line is a rlowss.

Early Holocene : Minimal ice shelf cavity development and grounded ice in inner Ross Sea region

Mid-Holocene: Transient retreat event(s) in the Ross Sea and establishment of Ross Ice Shelf cavity

Late-Holocene: Reduced meltwater, but enhanced ice-ocean feedbacks beneath greatly expanded Ross Ice Shelf cavity

854
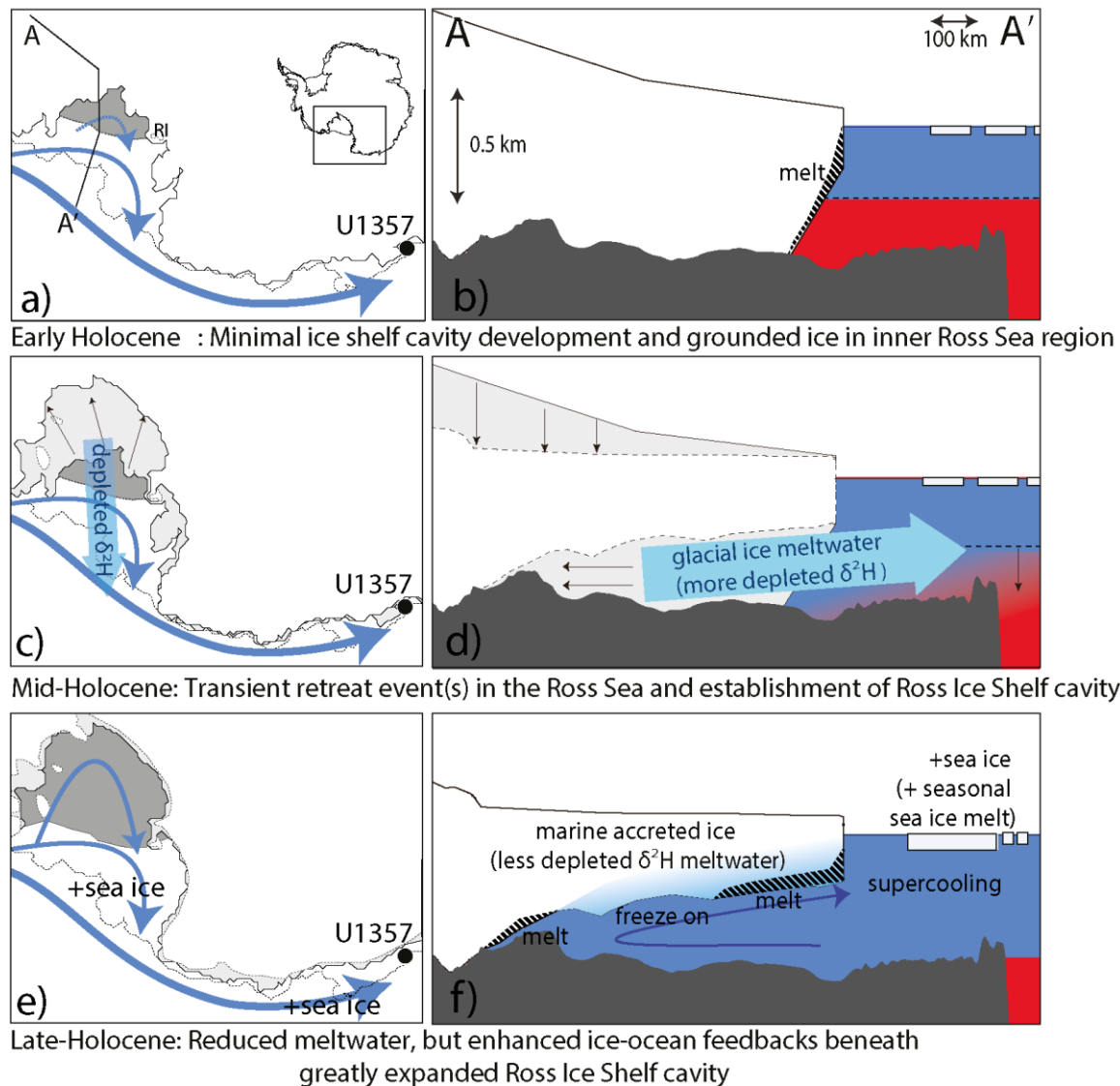
Figure 6: Conceptual model of evolving Holocene glacial and oceanographic conditions in the Ross Sea region. Panels on the left show modelled grounding line positions (McKay *et al.*, 2016), and proposed circulation of surface and sub-ice shelf circulating waters (light blue arrows). Panels on the right show cross sections of the Ross Ice Shelf (RIS) and ice-ocean interactions. Dark blue = cool surface waters, Red = warm subsurface waters. a) The grounding line in Adélie Land is near its modern location, but near Ross Island (RI) in the Ross Sea, and ice shelf cavity (dark grey shading) is reduced in size relative to today (McKay *et al.*, 2016). b) Continental shelf profile A-A' (panel a) shows a Ross Sea grounding line in a mid-continental shelf location in close proximity to the RIS calving line (McKay *et al.*, 2016), with subsurface warming on the continental shelf triggering WAIS deglaciation (Hillenbrand

et al., 2017). c) Most grounding line retreat south of RI occurred between 9 and 4.5 ka (light grey shading with black arrows represents area of retreat over this period), proposed to be the consequence of marine ice sheet instability, but the ice shelf calving line remained near its present position (McKay *et al.*, 2016; Spector *et al.*, 2017). d) Grounding line retreat and ice shelf thinning released meltwater with negative $\delta^2 H$ into the surface waters. Increasing ice shelf-oceanic interactions with the development of the ice shelf cavity (dark grey) led to enhanced Antarctic Surface Water formation; f) Minimal grounding line retreat has occurred since 4.5 ka, and the RIS supercools AASW leading to enhanced sea-ice formation despite reduced glacial meltwater flux. Seasonal sea ice meltwater further freshens and cools AASW. Increased production of AASW on the continental shelf leads to isopycnal deepening (dotted line) and limits flow onto the continental shelf slowing further grounding line retreat. However, as the ice shelf is near steady state mass balance and there is a component of marine accreted ice at the base of the ice shelf (Rignot *et al.*, 2013), the strength of the $\delta^2 H$ signal is reduced relative to periods of mass balance loss.
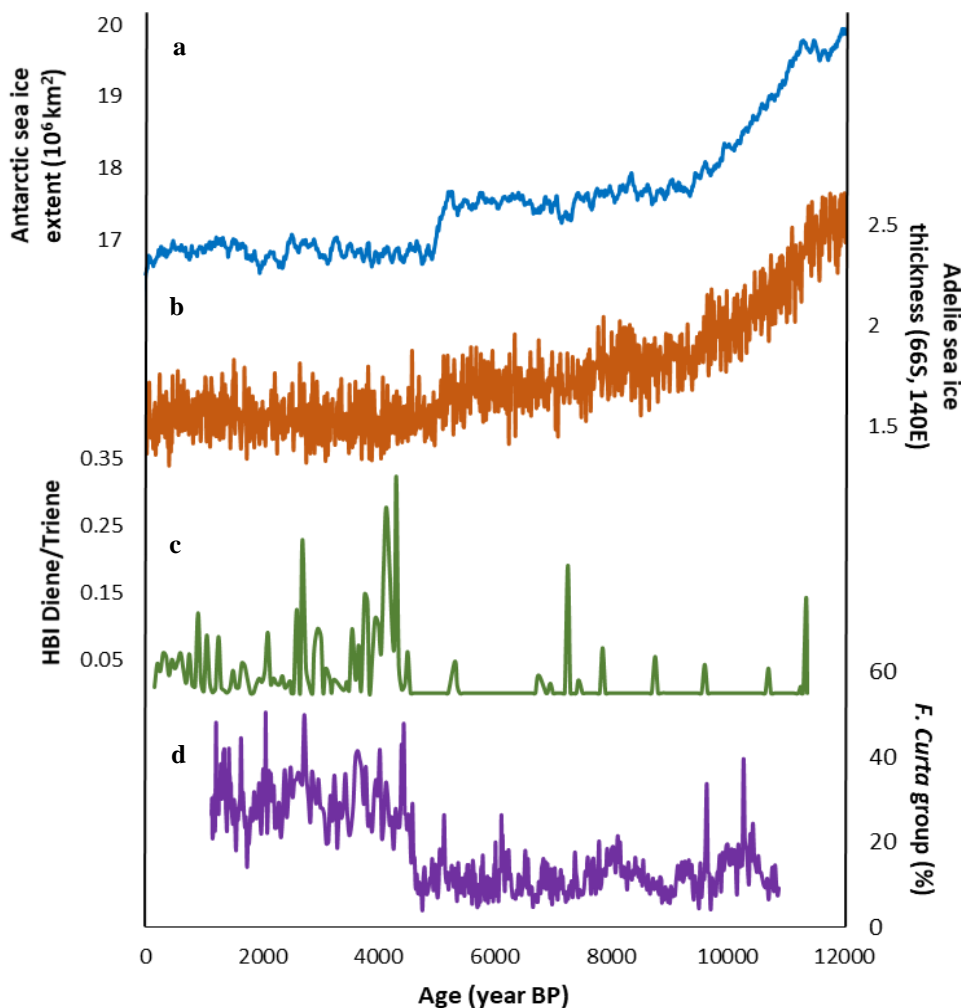
Figure 7 Comparison of sea ice data from the Adélie region with TraCE-21k simulations a) Antarctic sea ice extent (10^6 km^2) from TraCE-21k b) Adélie sea ice thickness (66°S, 140°E) from TraCE-21k c) Ratio of the di-unsaturated HBI (C25:2; Diene) and the tri-unsaturated HBI isomer (C25:3; Triene) at Site U1357 d) *Fragilariopsis curta* group relative abundances from MD03-2601.

878
879
880 **References:**
881

882 Adcroft, A. *et al.* (2004) 'Implementation of an Atmosphere–Ocean General Circulation Model on the
883 Expanded Spherical Cube', *Monthly Weather Review*, 132(12), pp. 2845–2863. doi:
884 10.1175/MWR2823.1.

885 Anderson, J. B. *et al.* (2014) 'Ross Sea paleo-ice sheet drainage and deglacial history during and since
886 the LGM', *Quaternary Science Reviews*. Elsevier Ltd, 100, pp. 31–54. doi:
887 10.1016/j.quascirev.2013.08.020.

888 Aoki, S. *et al.* (2013) 'Widespread freshening in the Seasonal Ice Zone near 140°E off the Adélie Land

Coast, Antarctica, from 1994 to 2012', *Journal of Geophysical Research: Oceans*, 118(11), pp. 6046–6063. doi: 10.1002/2013JC009009.

Arrigo, K. R. and van Dijken, G. L. (2003) 'Phytoplankton dynamics within 37 Antarctic coastal polynya systems', *Journal of Geophysical Research*, 108(C8), p. 3271. doi: 10.1029/2002JC001739.

Asper, V. L. and Smith, W. O. (1999) 'Particle fluxes during austral spring and summer in the southern Ross Sea, Antarctica', *Journal of Geophysical Research: Oceans*, 104(C3), pp. 5345–5359. doi: 10.1029/1998JC900067.

Baggenstos, D. *et al.* (2018) 'A Horizontal Ice Core From Taylor Glacier, Its Implications for Antarctic Climate History, and an Improved Taylor Dome Ice Core Time Scale', *Paleoceanography and Paleoclimatology*, 33(7), pp. 778–794. doi: 10.1029/2017PA003297.

Beans, C. *et al.* (2008) 'A study of the diatom-dominated microplankton summer assemblages in coastal waters from Terre Adelie to the Mertz Glacier, East Antarctica (139??E-145??E)', *Polar Biology*, 31(9), pp. 1101–1117. doi: 10.1007/s00300-008-0452-x.

Belt, S. T. *et al.* (2007) 'A novel chemical fossil of palaeo sea ice: IP25', *Organic Geochemistry*, 38(1), pp. 16–27. doi: 10.1016/j.orggeochem.2006.09.013.

Belt, S.T., Smik, L., Brown, T.A., et al. (2016) Source identification and distribution reveals the potential of the geochemical Antarctic sea ice proxy IPSO25. Nature Communications, 7: 12655. doi:10.1038/ncomms12655.

Bentley, M. J. *et al.* (2014) 'A community-based geological reconstruction of Antarctic Ice Sheet deglaciation since the Last Glacial Maximum', *Quaternary Science Reviews*, 100, pp. 1–9. doi: 10.1016/j.quascirev.2014.06.025.

Berger, A. and Loutre, M. F. (1991) 'Insolation values for the climate of the last 10 million years', *Quaternary Science Reviews*, 10(4), pp. 297–317. doi: 10.1016/0277-3791(91)90033-Q.

Bindoff, N., Rintoul, S. and Massom, R. (2000) 'Bottom water formation and polynyas in Adelie Land, Antarctica', *Papers and Proceedings of the Royal Society of Tasmania*, 133(3), pp. 51–56. doi: 10.26749/rstpp.133.3.51.

Brook, E. J. *et al.* (2005) 'Timing of millennial-scale climate change at Siple Dome, West Antarctica, during the last glacial period', *Quaternary Science Reviews*, 24(12–13), pp. 1333–1343. doi: 10.1016/j.quascirev.2005.02.002.

Budge, S. M. *et al.* (2008) 'Tracing carbon flow in an arctic marine food web using fatty acid-stable isotope analysis', *Oecologia*, 157(1), pp. 117–129. doi: 10.1007/s00442-008-1053-7.

Campagne, P. *et al.* (2015) 'Glacial ice and atmospheric forcing on the Mertz Glacier Polynya over the past 250 years', *Nature Communications*, 6. doi: 10.1038/ncomms7642.

Condron, A. and Winsor, P. (2012) 'Meltwater routing and the Younger Dryas', *Proceedings of the National Academy of Sciences*, 109(49), pp. 19928–19933. doi: 10.1073/pnas.1207381109.

924 Conway, H., Hall, B.L., Denton, G.H., et al. (1999) Past and Future Grounding-Line Retreat of the West
925 Antarctic Ice Sheet. Science, 286 (5438): 280–283. doi:10.1126/science.286.5438.280.

926 Crosta, X., Denis, D. and Ther, O. (2008) 'Sea ice seasonality during the Holocene, Adelie Land, East
927 Antarctica', *Marine Micropaleontology*, 66(3–4), pp. 222–232. doi: 10.1016/j.marmicro.2007.10.001.

928 Dalsgaard, J. *et al.* (2003) 'Fatty acid trophic markers in the pelagic marine environment', *Advances in
929 Marine Biology*, 46, pp. 225–340. doi: 10.1016/S0065-2881(03)46005-7.

930 DeMaster, D. J. (1981) 'The supply and accumulation of silica in the marine environment', *Geochimica
931 et Cosmochimica Acta*, 45(10), pp. 1715–1732. doi: 10.1016/0016-7037(81)90006-5.

932 Denis, D. *et al.* (2010) 'Sea ice and wind variability during the Holocene in East Antarctica: Insight on
933 middle-high latitude coupling', *Quaternary Science Reviews*, 29(27–28), pp. 3709–3719. doi:
934 10.1016/j.quascirev.2010.08.007.

935 DiTullio, G. R. *et al.* (2000) 'Rapid and early export of Phaeocystis antarctica blooms in the Ross Sea,
936 Antarctica', *Nature*, 404(6778), pp. 595–598. doi: 10.1038/35007061.

937 Domack, E. *et al.* (2006) 'Subglacial morphology and glacial evolution of the Palmer deep outlet
938 system, Antarctic Peninsula', *Geomorphology*, 75(1–2 SPEC. ISS.), pp. 125–142. doi:
939 10.1016/j.geomorph.2004.06.013.

940 Escutia, C. *et al.* (2011) 'Expedition 318 summary', in. doi: 10.2204/iodp.proc.318.101.2011.

941 Etourneau, J. *et al.* (2013) 'Holocene climate variations in the western Antarctic Peninsula: Evidence for
942 sea ice extent predominantly controlled by changes in insolation and ENSO variability', *Climate of the
943 Past*, 9(4), pp. 1431–1446. doi: 10.5194/cp-9-1431-2013.

944 Feakins, S. J., Warny, S. and Lee, J.-E. (2012) 'Hydrologic cycling over Antarctica during the middle
945 Miocene warming', *Nature Geoscience*, 5. doi: 10.1038/NGEO1498.

946 Hein, A. S. *et al.* (2016) 'Mid-Holocene pulse of thinning in the Weddell Sea sector of the West
947 Antarctic ice sheet', *Nature Communications*. Nature Publishing Group, 7, p. 12511. doi:
948 10.1038/ncomms12511.

949 Hellmer, H. H. (2004) 'Impact of Antarctic ice shelf basal melting on sea ice and deep ocean properties',
950 *Geophysical Research Letters*, 31(10), pp. 1–4. doi: 10.1029/2004GL019506.

951 Hillenbrand, C. D. *et al.* (2017) 'West Antarctic Ice Sheet retreat driven by Holocene warm water
952 incursions', *Nature*, 547(7661), pp. 43–48. doi: 10.1038/nature22995.

953 Hodell, D. A. *et al.* (2001) 'Abrupt Cooling of Antarctic Surface Waters and Sea Ice Expansion in the
954 South Atlantic Sector of the Southern Ocean at 5000 cal yr B.P.', *Quaternary Research*, 56(02), pp.
955 191–198. doi: 10.1006/qres.2001.2252.

956 Holland, D. M., Jacobs, S. S. and Jenkins, A. (2003) 'Modelling the ocean circulation beneath the Ross
957 Ice Shelf', *Antarctic Science*, 15(1), pp. 13–23. doi: 10.1017/S0954102003001019.

Huang, Y. *et al.* (1999) 'Glacial-interglacial environmental changes inferred from molecular and compound-specific δ13C analyses of sediments from Sacred Lake, Mt. Kenya', *Geochimica et Cosmochimica Acta*, 63(9), pp. 1383–1404. doi: 10.1016/S0016-7037(99)00074-5.

Hughes, K. *et al.* (2014) 'Extension of an Ice ShelfWater plumemodel beneath sea ice with application inMcMurdo Sound, Antarctica', *Journal of Geophysical Research: Oceans*, 119, pp. 8662–8687. doi: 10.1002/2014JC010248.Received.

Jacobs, S. S. *et al.* (2004) *Summer Oceanographic Measurements near the Mertz Polynya (140-150E) on NB Palmer Cruise 00-08*. doi: 10.15784/601161.

Jacobs, S. S., Giulivi, C. F. and Mele, P. A. (2002) 'Freshening of the Ross Sea During the Late 20th Century', *Science*, 297(5580), pp. 386–389. doi: 10.1126/science.1069574.

Jensen, S., Renberg, L. and Reutergårdh, L. (1977) 'Residue Analysis of Sediment and Sewage Sludge for Organochlorines in the Presence of Elemental Sulfur', *Analytical Chemistry*, 49(2), pp. 316–318. doi: 10.1021/ac50010a033.

Johns, L. *et al.* (1999) 'Identification of a C25highly branched isoprenoid (HBI) diene in Antarctic sediments, Antarctic sea-ice diatoms and cultured diatoms', *Organic Geochemistry*, 30(11), pp. 1471–1475. doi: 10.1016/S0146-6380(99)00112-6.

Jones, J. M. *et al.* (2016) 'Assessing recent trends in high-latitude Southern Hemisphere surface climate', *Nature Climate Change*. Nature Publishing Group, 6(10), pp. 917–926. doi: 10.1038/nclimate3103.

Jourdain, N. C. *et al.* (2017) 'Ocean circulation and sea-ice thinning induced bymelting ice shelves in the Amundsen Sea', *Journal of Geophysical Research: Oceans*, 122(3), pp. 2550–2573. doi: 10.1002/2016JC012509.Received.

Killops, S. and Killops, V. (2004) *Introduction to Organic Geochemistry*, *Blackwell Publishing Ltd.* doi: 10.1002/9781118697214.

Kim, J. H. *et al.* (2002) 'Interhemispheric comparison of deglacial sea-surface temperature patterns in Atlantic eastern boundary currents', *Earth and Planetary Science Letters*, 194(3–4), pp. 383–393. doi: 10.1016/S0012-821X(01)00545-3.

Kim, J. H. *et al.* (2010) 'New indices and calibrations derived from the distribution of crenarchaeal isoprenoid tetraether lipids: Implications for past sea surface temperature reconstructions', *Geochimica et Cosmochimica Acta*, 74(16), pp. 4639–4654. doi: 10.1016/j.gca.2010.05.027.

Kingslake, J., Scherer, R.P., Albrecht, T., et al. (2018) Extensive retreat and re-advance of the West Antarctic Ice Sheet during the Holocene. Nature, 558 (7710): 430–434. doi:10.1038/s41586-018-0208-x.

Kopczynska, E. E. *et al.* (1995) 'Phytoplankton Composition and Cell Carbon Distribution in Prydz Bay, Antarctica - Relation To Organic Particulate Matter and Its Delta-C-13 Values', *Journal of Plankton Research*, 17(4), pp. 685–707. doi: 10.1093/plankt/17.4.685.

993   Kusahara, K., Hasumi, H. and Tamura, T. (2010) 'Modeling sea ice production and dense shelf water
994   formation in coastal polynyas around East Antarctica', *Journal of Geophysical Research: Oceans*,
995   115(10), p. C10006. doi: 10.1029/2010JC006133.

996   Leventer, A. *et al.* (2006) 'Marine sediment record from the East Antarctic margin reveals dynamics of
997   ice sheet recession', *GSA Today*, 16(12), pp. 4–10. doi: 10.1130/GSAT01612A.1.

998   Liu, Z. *et al.* (2014) 'The Holocene temperature conundrum', *Proceedings of the National Academy of*
999   *Sciences*, 111(34), pp. E3501--E3505. doi: 10.1073/pnas.1407229111.

1000   Lowry, D. P. *et al.* (2019) 'Deglacial grounding-line retreat in the Ross Embayment, Antarctica,
1001   controlled by ocean and atmosphere forcing', *Science Advances*. doi: 10.1126/sciadv.aav8754.

1002   Mackintosh, A. N. *et al.* (2014) 'Retreat history of the East Antarctic Ice Sheet since the Last Glacial
1003   Maximum', *Quaternary Science Reviews*. Elsevier Ltd, 100, pp. 10–30. doi:
1004   10.1016/j.quascirev.2013.07.024.

1005   Marcott, S. a. *et al.* (2013) 'A Reconstruction of Regional and Global Temperature for the Past 11,300
1006   Years', *Science (New York, N.Y.)*, 339(6124), pp. 1198–1201. doi: 10.1126/science.1228026.

1007   Marshall, J. *et al.* (1997) 'A finite-volume, incompressible Navier Stokes model for studies of the ocean
1008   on parallel computers', *Journal of Geophysical Research: Oceans*, 102(C3), pp. 5753–5766. doi:
1009   10.1029/96JC02775.

1010   Marsland, S. J. *et al.* (2004) 'Modeling water mass formation in the Mertz Glacier Polynya and Ad??lie
1011   Depression, East Antarctica', *Journal of Geophysical Research: Oceans*, 109(11), p. C11003. doi:
1012   10.1029/2004JC002441.

1013   Massé, G. *et al.* (2011) 'Highly branched isoprenoids as proxies for variable sea ice conditions in the
1014   Southern Ocean', *Antarctic Science*, 23(5), pp. 487–498. doi: 10.1017/S0954102011000381.

1015   Massom, R. A. *et al.* (2001) 'Effects of regional fast-ice and iceberg distributions on the behaviour of
1016   the Mertz Glacier polynya, East Antarctica', *Annals of Glaciology*, 33, pp. 391–398. doi:
1017   10.3189/172756401781818518.

1018   Massom, R. A. *et al.* (2018) 'Antarctic ice shelf disintegration triggered by sea ice loss and ocean swell',
1019   *Nature*. Springer US, (Ii). doi: 10.1038/s41586-018-0212-1.

1020   Masson-Delmotte, V. *et al.* (2011) 'A comparison of the present and last interglacial periods in six
1021   Antarctic ice cores', *Climate of the Past*, 7(2), pp. 397–423. doi: 10.5194/cp-7-397-2011.

1022   Matsuda, H. (1978) 'Early diagenesis of fatty acids in lacustrine sediments-III. Changes in fatty acid
1023   composition in the sediments from a brackish water lake', *Geochimica et Cosmochimica Acta*, 42, pp.
1024   1027–1034.

1025   Mayer, L. M. (1993) 'Organic Matter at the Sediment-Water Interface', in *Organic Geochemistry:*
1026   *principles and applications*, pp. 171–184. doi: 10.1007/978-1-4615-2890-6_7.

1027 McCartney, M. S. and Donohue, K. A. (2007) 'A deep cyclonic gyre in the Australian-Antarctic Basin',
1028 *Progress in Oceanography*, 75(4), pp. 675–750. doi: 10.1016/j.pocean.2007.02.008.

1029 McCave, I. N. and Hall, I. R. (2006) 'Size sorting in marine muds: Processes, pitfalls, and prospects for
1030 paleoflow-speed proxies', *Geochemistry, Geophysics, Geosystems*, 7(10). doi: 10.1029/2006GC001284.

1031 McCave, I. N., Manighetti, B. and Robinson, S. G. (1995) 'Sortable silt and fine sediment
1032 size/composition slicing: Parameters for palaeocurrent speed and palaeoceanography',
1033 *Paleoceanography*, 10(3), pp. 593–610. doi: 10.1029/94PA03039.

1034 McKay, R. *et al.* (2016) 'Antarctic marine ice-sheet retreat in the Ross Sea during the early Holocene',
1035 *Geology*, 44(1), pp. 7–10. doi: 10.1130/G37315.1.

1036 Meyers, P. A. and Ishiwatari, R. (1993) 'Lacustrine organic geochemistry-an overview of indicators of
1037 organic matter sources and diagenesis in lake sediments', *Organic Geochemistry*, 20(7), pp. 867–900.
1038 doi: 10.1016/0146-6380(93)90100-P.

1039 Mezgec, K. *et al.* (2017) 'Holocene sea ice variability driven by wind and polynya efficiency in the Ross
1040 Sea', *Nature Communications*. Springer US, 8(1). doi: 10.1038/s41467-017-01455-x.

1041 Nielsen, S. H. H. *et al.* (2007) 'Origin and significance of ice-rafted detritus in the Atlantic sector of the
1042 Southern Ocean', *Geochemistry, Geophysics, Geosystems*, 8(12), p. n/a-n/a. doi:
1043 10.1029/2007GC001618.

1044 Pagani, M. *et al.* (2006) 'Arctic hydrology during global warming at the Palaeocene/Eocene thermal
1045 maximum', *Nature*, 442(7103), pp. 671–675. doi: 10.1038/nature05043.

1046 Paolo, F. S., Fricker, H. A. and Padman, L. (2015) 'Volume loss from Antarctic ice shelves is
1047 accelerating', *Science*, 348(6232), pp. 327–331. doi: 10.1126/science.aaa0940.

1048 Peña-Molino, B., McCartney, M. S. and Rintoul, S. R. (2016) 'Direct observations of the Antarctic
1049 Slope Current transport at 113°E', *Journal of Geophysical Research: Oceans*. doi:
1050 10.1002/2015JC011594.

1051 Peters, K. E. and Moldowan, J. M. (1993) 'The biomarker guide: interpreting molecular fossils in
1052 petroleum and ancient sediments', *The biomarker guide: interpreting molecular fossils in petroleum and
1053 ancient sediments*. doi: 10.5860/choice.30-2690.

1054 Pollard, D. and Deconto, R. M. (2016) 'Contribution of Antarctica to past and future sea-level rise',
1055 *Nature*, 531(7596), pp. 591–597. doi: 10.1038/nature17145.

1056 Potter, J. R. and Paren, J. G. (1985) 'Interaction between ice shelf and ocean in George VI Sound,
1057 Antarctica', in *Oceanology of the Antarctic Continental Shelf (ed S. S. Jacobs)*, pp. 35–58. doi:
1058 10.1029/AR043p0035.

1059 Rhodes, R. H. *et al.* (2012) 'Little Ice Age climate and oceanic conditions of the Ross Sea, Antarctica
1060 from a coastal ice core record', *Climate of the Past*, pp. 1223–1238. doi: 10.5194/cp-8-1223-2012.

Riaux-Gobin, C. *et al.* (2011) 'Spring phytoplankton onset after the ice break-up and sea-ice signature (Ade??lie Land, East Antarctica)', *Polar Research*, 30(SUPPL.1). doi: 10.3402/polar.v30i0.5910.

Riaux-Gobin, C. *et al.* (2013) 'Environmental conditions, particle flux and sympagic microalgal succession in spring before the sea-ice break-up in Adélie Land, East Antarctica', *Polar Research*, 32, pp. 0–25. doi: 10.3402/polar.v32i0.19675.

Rignot, E. *et al.* (2013) 'Ice Shelf Melting Around Antarctica', *Science*, 1(June), pp. 1–15. doi: 10.1126/science.1235798.

Riis, V. and Babel, W. (1999) 'Removal of sulfur interfering in the analysis of organochlorines by GC-ECD', *Analyst*, 124(12), pp. 1771–1773. doi: 10.1039/a907504f.

Robinson, N. J. *et al.* (2014) 'Evolution of a supercooled Ice Shelf Water plume with an actively growing subice platelet matrix', *Journal of Geophysical Research : Oceans*, pp. 3425–3446. doi: 10.1002/2013JC009399.Received.

Sachse, D. *et al.* (2012) 'Molecular Paleohydrology: Interpreting the Hydrogen-Isotopic Composition of Lipid Biomarkers from Photosynthesizing Organisms', *Annual Review of Earth and Planetary Sciences*, 40(1), pp. 221–249. doi: 10.1146/annurev-earth-042711-105535.

Schmidt, G. A., Bigg, G. R. and Rohling, E. J. (1999) *Global Seawater Oxygen-18 Database - v1.22*. Available at: https://data.giss.nasa.gov/o18data/.

Schoemann, V. *et al.* (2005) 'Phaeocystis blooms in the global ocean and their controlling mechanisms: A review', *Journal of Sea Research*, pp. 43–66. doi: 10.1016/j.seares.2004.01.008.

Schouten, S. *et al.* (2006) 'The effect of temperature, salinity and growth rate on the stable hydrogen isotopic composition of long chain alkenones produced by *Emiliania huxleyi* and *Gephyrocapsa oceanica*', *Biogeosciences*, 3(1), pp. 113–119. doi: 10.5194/bg-3-113-2006.

Sessions, A. L. *et al.* (1999) 'Fractionation of hydrogen isotopes in lipid biosynthesis, Org', *Organic Geochemistry*, 30, pp. 1193–1200. doi: 10.1016/S0146-6380(99)00094-7.

Sessions, A. L. *et al.* (2004) 'Isotopic exchange of carbon-bound hydrogen over geologic timescales', *Geochimica et Cosmochimica Acta*, 68(7), pp. 1545–1559. doi: 10.1016/j.gca.2003.06.004.

Shackleton, N. J. and Kennett, J. P. (1975) 'Paleotemperature history of the Cenozoic and the initiation of Antarctic glaciation; Oxygen and carbon isotope analyses in DSDP sites 277, 279 and 281', *Initial Reports of the Deep Sea Drilling Project*, 29, pp. 743–755. doi: 10.2973/dsdp.proc.37.1977.

Smethie, W. M. and Jacobs, S. S. (2005) 'Circulation and melting under the Ross Ice Shelf: Estimates from evolving CFC, salinity and temperature fields in the Ross Sea', *Deep-Sea Research Part I: Oceanographic Research Papers*, 52(6), pp. 959–978. doi: 10.1016/j.dsr.2004.11.016.

Smik, L., Belt, S.T., Lieser, J.L., et al. (2016) Distributions of highly branched isoprenoid alkenes and other algal lipids in surface waters from East Antarctica: Further insights for biomarker-based paleo sea-ice reconstruction. Organic Geochemistry, 95: 71–80. doi:10.1016/j.orggeochem.2016.02.011.

1097 Smith Jr., W. O. *et al.* (2012) 'the Ross Sea in a Sea of Change', *Oceanography*, 25(3, SI), pp. 90–103.

1098 Solomina, O. N. *et al.* (2015) 'Holocene glacier fluctuations', *Quaternary Science Reviews*, pp. 9–34.
1099 doi: 10.1016/j.quascirev.2014.11.018.

1100 Spector, P. *et al.* (2017) 'Rapid early-Holocene deglaciation in the Ross Sea, Antarctica', *Geophysical*
1101 *Research Letters*, 44(15), pp. 7817–7825. doi: 10.1002/2017GL074216.

1102 Steig, E. J. *et al.* (1998) 'Changes in climate, ocean and ice sheet conditions in the Ross Embayment at 6
1103 ka', *Annals of Glaciology*, 27, pp. 305–310. doi: 10.3198/1998AoG27-1-305-310.

1104 Strickland, J. D. and Parsons, T. R. (1970) 'J. D. H. Strickland and T. R. Parsons: A Practical Handbook
1105 of Seawater Analysis. Ottawa: Fisheries Research Board of Canada, Bulletin 167, 1968. 293 pp. $ 7.50',
1106 in *Internationale Revue der gesamten Hydrobiologie und Hydrographie*, pp. 167–167. doi:
1107 10.1002/iroh.19700550118.

1108 Tang, K. W. *et al.* (2008) 'Colony size of Phaeocystis antarctica (Prymnesiophyceae) as influenced by
1109 zooplankton grazers', *Journal of Phycology*, 44(6), pp. 1372–1378. doi: 10.1111/j.1529-
1110 8817.2008.00595.x.

1111 Todd, C., Stone, J., Conway, H., et al. (2010) Late Quaternary evolution of Reedy Glacier, Antarctica.
1112 Quaternary Science Reviews, 29 (11–12): 1328–1341. doi:10.1016/j.quascirev.2010.02.001.

1113 Turner, J. *et al.* (2016) 'Antarctic sea ice increase consistent with intrinsic variability of the Amundsen
1114 sea low', *Climate Dynamics*. Springer Berlin Heidelberg, 46(7–8), pp. 2391–2402. doi: 10.1007/s00382-
1115 015-2708-9.

1116 Wong, W. W. and Sackett, W. M. (1978) 'Fractionation of stable carbon isotopes by marine
1117 phytoplankton', *Geochimica et Cosmochimica Acta*, 42(12), pp. 1809–1815. doi: 10.1016/0016-
1118 7037(78)90236-3.

1119 Zhang, J. and Hibler, W. D. (1997) 'On an efficient numerical method for modeling sea ice dynamics',
1120 *Journal of Geophysical Research*, 102(C4), p. 8691. doi: 10.1029/96JC03744.

1121 Zhang, Z., Sachs, J. P. and Marchetti, A. (2009) 'Hydrogen isotope fractionation in freshwater and
1122 marine algae: II. Temperature and nitrogen limited growth rate effects', *Organic Geochemistry*, 40(3),
1123 pp. 428–439. doi: 10.1016/j.orggeochem.2008.11.002.

1124
1125

1126 **Acknowledgements:** Samples and data were provided by the International
1127 Ocean Discovery Program (IODP). The Natural Environment Research Council funded K.E.A (CENTA
1128 PhD; NE/L002493/1) and J.B. (Standard Grant Ne/I00646X/1). J.B. and O.S. were funded by Japanese
1129 Society for the Promotion of Science (JSPS/FF2/60 No. L-11523). R.M. and N.B were funded by the
1130 NZ Marsden Fund (18-VUW-089 and 15-VUW-131). A.C. was funded by the NSF (PLR-1443347) and
1131 the U.S. Dept. of Energy (DE-SC0016105). A.C. performed model integrations at the National Research
1132 Scientific Computing Center and at XSEDE, an NSF funded computer center (grant ACI-1548562).
1133 C.R. was funded by a L'Oréal-UNESCO New Zealand For Women in Science Fellowship, University of

1134   Otago Research Grant, and the IODP U.S. Science Support Program. We thank S. Schouten, V.
1135   Willmott, F. Sangiorgi, J. Toney and J. Pike for discussions and V. Willmott, H. Moossen, A. Hallander,
1136   R. Jamieson and C. Gallagher for technical support.

1137

1138   **Author contributions:** K.E.A., J.B and R.M. wrote the paper. J.B. and O.S. carried out the fatty acid
1139   isotope analysis, A.A. and R.M. conducted the grain size analyses, J.E. and G.M. generated the HBI
1140   data, F.J.J.E measured X-ray fluorescence scanning and electron microscopy, and C.R conducted the
1141   opal measurements. R.D., R.M., X.C. and G.M. developed the age model. A.C ran the model
1142   simulations. D.P.L and E.G analysed the Trace-21k experiment data. R.D. was lead proponent on the
1143   U1357 drilling proposal. All authors contributed to the interpretations of data and finalization of the
1144   manuscript.

1145

1146   **Competing interests:** The authors have no competing interests.

1147

1148   **Data availability:** There is no restriction on data availability. Upon manuscript acceptance, all
1149   previously unpublished data will be added to the Supplementary Materials and made freely available at
1150   the NOAA NCDC data-base: https://www.ncdc.noaa.gov/data-access/paleoclimatology-data/datasets.

1151

1152

1153

1154